Solid Earth

Open Access

Discussions

EGU

Fluid-mediated, brittle-ductile deformation at seismogenic depth: Part II – Stress history and fluid pressure variations in a shear zone in a nuclear waste repository (Olkiluoto Island, Finland)

5   Francesca Prando[1], Luca Menegon[1,2], Mark. W. Anderson[1], Barbara Marchesini[3], Jussi Mattila [4,5] and Giulio Viola[3]

[1] School of Geography, Earth and Environmental Sciences, University of Plymouth, PL48AA Plymouth, UK
[2] The Njord Centre, Department of Geoscience, University of Oslo, P.O. Box 1048 Blindern, Norway
10   [3] Dipartimento di Scienze Biologiche, Geologiche e Ambientali, Università di Bologna, Italy
[4] Geological Survey of Finland, Espoo, Finland
[5] Currently at: Rock Mechanics Consulting Finland Oy (RMCF), Vantaa, Finland

Correspondence to: Francesca Prando (francesca.prando@plymouth.ac.uk) and Luca Menegon
15   (luca.menegon@plymouth.ac.uk)

Abstract. Microstructural record of fault rocks active at the brittle ductile transition zone (BDTZ) may retain information on the rheological parameters driving the switch in deformation mode, and on the role of stress and fluid pressure in controlling different fault slip behaviours. In this study we analysed the deformation microstructures of the strike-slip fault zone BFZ045
20   in Olkiluoto (SW Finland), located in the site of a deep geological repository for nuclear waste. We combined microstructural analysis, electron backscatter diffraction (EBSD), and mineral chemistry data to reconstruct the variations in pressure, temperature, fluid pressure and differential stress that mediated deformation and strain localization along BFZ045 across the BDTZ. BFZ045 exhibits a mixed ductile-brittle deformation, with a narrow (< 20 cm thick) brittle fault core with cataclasites and pseudotachylytes that overprint a wider (60-100 cm thick) quartz-rich mylonite. Ductile deformation took place at 400-
25   500° C and 3-4 kbar, typical of the greenschist facies metamorphism at the base of the seismogenic crust. Cataclastic deformation occurred under lower T conditions down to T ≥ 320° C and was not further overprinted by mylonitic creep. We used the recrystallized grain size piezometry for quartz to document a progressive increase in differential stress during mylonitization, from ca. 50 MPa to ca. 120 MPa. The increase in differential stress was localised towards the shear zone centre, which was eventually overprinted by brittle deformation in a narrowing shear zone. Synkinematic quartz veins emplaced along
30   the mylonitic foliation during an early, low stress creep event, and were overprinted by dynamic recrystallization and mylonitic creep at increasing differential stress. We propose a conceptual model in which the ductile-brittle deformation cycle was

controlled by transient oscillations in fluid pressure in a narrowing shear zone deforming at progressively higher differential stress during cooling.

35 **1 Introduction**

The change from fracturing and frictional sliding to dominant thermally activated creep processes accommodating viscous flow in mylonitic rocks occurs at the brittle–ductile transition zone (BDTZ; e.g. Kohlstedt et al., 1995; Handy et al., 2007). Conventional strength envelopes localize the BDTZ at a depth of 10-15 km in the continental crust (Kohlstedt et al., 1995, Ranalli, 1997, Bos and Spiers, 2002), corresponding to the base of the seismogenic zone (Sibson, 1982). Strength envelopes

40 also predict that the BDTZ coincides with a peak strength in the crust, between the brittle upper crust and the ductile middle- and lower crust. Naturally constrained stress profiles through exhumed mid-crustal rocks are consistent with this picture (Behr and Platt, 2011).

However, field evidence of seismic behaviour followed by solid-state viscous creep below the brittle-ductile transition in the continental crust (Austrheim, 2013, Menegon et al., 2017; White 1996, 2012), as well as of the cyclical interplay between

45 brittle and ductile deformation during the evolution of mid-crustal shear zones (e.g. Pennacchioni and Mancktelow, 2007; Fusseis and Handy, 2008; Wehrens et al., 2016; Melosh et al., 2018), demonstrate that the BDTZ occupies a depth interval that can vary transiently reflecting changes in, e.g., stress and fluid pressure, as well as changes in shear zone- and fault microstructures (Handy et al., 2007). More specifically, different deformation mechanisms (dislocation creep, diffusion creep, fluid-assisted veining, dissolution-precipitation creep, fracturing and cataclasis) overlap in space and time at the BDTZ as a

50 function of lithology, P-T conditions, and oscillating stress, strain rate and fluid pressure. Thus, the BDTZ occurs over a relatively wide range of conditions in a depth interval marked by significant fluctuations in strength (Hirth and Tullis, 1994; Scholz, 1998; Fossen and Cavalcante, 2017; Melosh et al., 2018) and fluid pressure (Cox, 2010; Kjøll et al, 2015; Sibson and Rowland, 2003; Yardley and Baumgartner, 2007; Marchesini et al., 2019) that steer the overall short- and long-term rheological behaviour of the crust. Given that shear zones at the BDTZ act as rheologically weak detachment horizons within the crust

55 (Handy and Brun, 2004; Gueydan et al., 2003; Pfiffner, 2016), understanding the effects of stress-, strain rate- and fluid pressure fluctuations on the rheological evolution of shear zones at the BDTZ is an important goal in tectonics research. In particular, it is important to assess whether evidence of such cyclical fluctuations are preserved in the geological record, and whether the extent of such variations can be estimated by examining natural fault rocks.

Microstructures can record crucial information on the parameters steering deformation cycles at the BDTZ, and are an

60 invaluable tool that enables derivation of rheological parameters of shear zones (e.g. Stipp et al., 2002; Behr and Platt, 2011; Ceccato et al., 2018). However, the mutual overprinting relationships between brittle and ductile deformation and associated fault rocks at the BDTZ typically result in only partial microstructural records, in which the youngest deformation event might have completely overprinted the evidence of earlier deformation episodes. Recent deformation experiments have, however,

opened up new avenues for the detailed investigations of natural deformation microstructures in quartz-rich rocks that result

65   from stress variations during brittle-ductile deformation. The 'kick and cook' experiments have documented quartz microstructures formed during transient high stress deformation followed by stress relaxation (Trepmann et al., 2007). Similar microstructures found in natural shear zones formed below the BDTZ were interpreted to results from seismic loading from the overlying brittle crust, followed by either static grain growth or dislocation creep deformation at relaxing stress (Trepmann and Stöckhert, 2003, 2013; Trepmann et al., 2017). Deformation experiments conducted by Kidder et al. (2016) show that the

70   microstructure associated with a stress increase in quartzite is a bimodal distribution of recrystallized grain size. The smaller grains accurately record the stress increase, whereas the surviving coarser grains formed during earlier, lower stress deformation. The smaller grains can be used to constrain differential stresses during the most recent (high stress) deformation event using a recrystallized grain size palaeopiezometer (Stipp and Tullis, 2003; Cross et al., 2017).

Fluids can also play a fundamental role in triggering a transient switch from dominantly ductile to brittle deformation, as

75   demonstrated for example by the synkinematic emplacement of quartz veins subsequently overprinted by crystal-plastic deformation (Handy et al., 2007; Kjøll et al., 2015; Trepmann and Seybold 2019; Marchesini et al., 2019). Cyclical ductile-brittle-ductile deformation associated with high fluid fluxes involving a fault-valve behaviour (Sibson, 1990) implies cycles of fluid pressure build-up followed by fluid venting and pressure drop, and has been related to seismic fault behaviour (Sibson, 1992; Cox, 1995; Nguyen at al., 1998; Viola et al., 2006). Near lithostatic values of fluid pressure are required to facilitate

80   synkinematic vein emplacement in a shear zone at the BDTZ (Cox, 1995; Streit and Cox, 2001; Cox, 2007; Hirth and Beeler, 2015).

Given the fundamental interplay between variations in P-T conditions, fluid pressures, stress and strain rate occurring at the BDTZ, fault modelling and field studies must attempt to quantify the thermal and structural history of fault rocks, as well as the fluid activity in faults in order to untangle the relative contribution of different rheological parameters in controlling the

85   dominant deformation mode and mechanisms active at seismogenic depths. This study investigates the microstructural record of the deformation behaviour at the BDTZ of a subvertical sinistral strike-slip fault hosted in granitoids of the Paleoproterozoic Baltic Shield in Finland. The fault occurs within the deep ONKALO spent nuclear fuel repository that is currently being built on the island of Olkiluoto in SW Finland (Fig. 1a). The present-day structure of the fault consists of a narrow (< 20 cm thick) brittle fault zone core that exploits a wider (ca. 1 m thick) ductile, mylonitic precursor. We constrain the deformation history

90   of the fault zone and use quartz microstructure to estimate the stress history of the mylonitic precursor. We propose a conceptual model of the evolution of fault slip behaviour that incorporates the constraints on differential stress and fluid pressure derived from our microstructural analysis, and that favours the scenario of a narrowing shear zone that progressively localizes strain when deforming across the BDTZ.

2 Geological Setting

95   The island of Olkiluoto in SW Finland (Fig. 1a) is located in the Paleoproterozoic bedrock of the Baltic shield. The region is dominated by high grade metasediments and by plutonic rocks, emplaced during the latest accretionary stages of the Svecofennian Orogeny between 1.89 and 1.80 Ga (Lahtinen et al 1994, Nironen et al. 1997, Lahtinen et al 2005, Pajunen et al. 2008). In the study area, the dominant rock types consist of amphibolite facies migmatitic metasediments, calc-alkaline synorogenic TTG-type granitoids, and late-orogenic leucogranites and pegmatites. The migmatisation occurred between 1.84-

100   1.82 Ga (Aaltonen et al. 2016), during the collisional stage of the Svecofennian Orogeny characterized by considerable crustal thickening and high-grade metamorphism (Kukkonen and Lauri, 2009). Stable mineral assemblages constrain the formation of the migmatite at 3.7-4.2 Kbar and 660-700° C (Tuisku and Karki, 2010). Tonalite and granodiorite intrusions were emplaced prior to the metamorphic peak, between 1.89 and 1.85 Ma (Mänttäri et al., 2006), while leucogranites intrusions emplaced during the high-grade metamorphism and late orogenic stages, between 1.85 to 1.79 Ga (Mänttäri et al., 2010). Retrograde

105   metamorphism under greenschist facies conditions affected the rocks soon after the peak conditions, and continued throughout the orogenic collapse, dated at 1.79-1.77 Ga for SW Finland (Lahtinen et al., 2005). Approximately 150 Ma later, during an extensional tectonic phase, Southern Finland was intruded by Rapakivi granites (1.65-1.54 Ga), with the Laitila and Eurajoki plutons located at 15 and 4 km eastern of Olkiluoto, respectively. Crustal extension also caused the formation of an NW–SE trending graben 50 km north of Olkiluoto, later filled with Mesoproterozoic sandstones. Olkiluoto bedrock was affected by the

110   emplacement of NE-SW striking diabase dykes (1.56 Ga) and Greisen veins associated with the Rapakivi batholiths intrusions and graben formation. The intrusion of olivine diabase sills occurred during a phase of regional compression at c. 1.27-1.25 Ga (Suominen 1991).

The study area was affected by a polyphase ductile deformation between 1.86 and 1.79 Ga (Aaltonen et al., 2016), followed by a complex brittle deformation history, as a result of exhumation and cooling. Aaltonen et al. (2010) identified characteristic

115   structures for three (D_2-D_4) deformation stages, which overprint a pre-migmatite, poorly preserved deformation stage (D_1). At 1.86-1.83 Ga, D_2 deformation affected progressively the bedrock of Olkiluoto, developing a pervasive NE-SW striking high-grade (locally migmatitic) foliation dipping moderately towards SE, as well as NE–SW striking mesoscopic shear zones (Aaltonen et al. 2010). The following D_3 stage (1.83 to 1.81 Ga) was more localized and occurred under amphibolite facies conditions. It resulted in NNE-SSW striking foliations, observed in the central part of Olkiluoto, and E-W to NE-SW trending,

120   S to SE dipping shear zones (Aaltonen at al. 2010). The latest stage, D_4, developed under greenschist facies retrograde metamorphism around 1.81–1.79 Ga according to U/Pb dating of syn-kinematic pegmatites (Mänttäri et al., 2010). D_4 structures consist of NNE-SSW and N-S striking subvertical ductile shear zones, varying in width from ~ 0.5 m to 200 m (Fig.1a).

The progressive regional exhumation led to a switch in deformation style, with the onset of brittle deformation in Olkiluoto at

125   ~ 1.75 Ga (Mattila and Viola, 2014, Aaltonen et al., 2016). Mattila and Viola (2014) used paleostress inversion of fault slip data to identify seven distinct brittle stages that developed in the time span from 1.75 to 0.8 Ga. These brittle deformation

stages are characterized by both the reactivation of optimally oriented pre-existing ductile structures, and by the formation of new Andersonian-type faults and joints. The dominant brittle structures in the study area can be grouped into two main sets: (1) an E-W to NE-SW trending set of low angle faults exploiting the regional migmatitic foliation, and (2) a set of subvertical

130   faults striking N-S to NW-SE (Fig.1; Aaltonen et al., 2016). We assumed that, previous to the brittle stage, the crust in Olkiluoto had been passively exhumed during the late- to post-orogenic deformation stages of the Svecofennian orogeny (Lahtinen et al., 2005). Low angle faults cross-cut the subvertical faults and attest to a later stage of exhumation (Aaltonen et al., 2016).

The subvertical faults have orientation compatible with the first stage of brittle deformation identified by Mattila and Viola

135   (2014), and they typically form conjugate systems of NNW–SSE sinistral and NW–SE dextral strike-slip faults (Mattila and Viola, 2014). This conjugate system has been interpreted to result from the NW–SE to NNW–SSE compression proposed for the late- to post- Svecofennian orogeny (Viola et al., 2009; Torvela and Ehlers, 2010; Saintot at al., 2011).

A network of vertical N-S and NW-SE faults has been mapped and investigated at the repository scale with underground surveys and boreholes (Aaltonen et al. 2016, Fig 1b). N-S faults are typically localized on mica-rich precursor ductile shear

140   zones (Pere, 2009). The role of subvertical, N-S striking ductile precursor zones in controlling the localization of faults at the disposal site was investigated by Skyttä and Torvela (2018), who identified the ductile precursor structures as short limbs of D_4 asymmetric folds and as anastomosing networks of discrete retrograde (greenschist facies) ductile shear zones. Skyttä and Torvela (2018) proposed that the subvertical N-S faults formed as a result of progressive strain localisation during the late stage of D_4 deformation, which culminated in the development of faults through linkage of individual fault segments that

145   preferentially exploited optimally oriented branches of the anastomosing network of localised ductile high strain zones. As such, the faults exploiting D_4 shear zones represent ideal targets to investigate the deformation processes and mechanisms at the brittle-ductile transition, and the associated rheological parameters recorded in the fault rock microstructures. This study uses the N-S sinistral strike-slip fault BFZ045 as a natural laboratory to investigate the stress history of the ductile precursor and the role of fluids on the deformation processes active at the brittle-ductile transition. The companion paper by Marchesini

150   et al. (2019) has thoroughly described the deformation history of the conjugate (yet very different) dextral BFZ300 fault.

3 Methods

Samples were obtained from two sub-horizontal drill cores from the underground facilities that intersect the BFZ045 fault (Fig. 2a). The analysed samples were selected from (i) a 2 m continuous section along drill core PH28, which was drilled at a depth of 433 m b.s.l. and is oriented ESE-WNW, and (ii) drill core PH16 from the Demonstration Facilities tunnels at 420 m

155   depth, described in Aaltonen et al. (2016). The PH28 samples were selected from the 99-101m interval of the drill core, with core distance measured from ESE to WNW, which includes the fault core and the proximal damage zone. The drill core was cut in half parallel to the stretching lineation and perpendicular to the mylonitic foliation and subsampled at regular intervals of 2 cm. Nineteen polished thin sections cut parallel to the stretching lineation were added to three samples from PH16

previously described in Aaltonen et al. (2016). An additional thin section from drill core PH21 (drilled at the same depth of
160 PH16) was used to estimate the T of the fabric formation in the host rock using Raman spectroscopy of carbonaceous material
(see 3.2 and 4.5).

3.1 Microstructural observations and Electron Backscatter Diffraction (EBSD) analysis

Deformation microstructures were investigated using petrographic microscopy and scanning electron microscopy (SEM). SEM
and EBSD analysis was performed at the Plymouth University Electron Microscopy Centre using a JEOL LV6610 SEM and
165 a JEOL 7001 FEG-SEM. Thin sections used for Electron Backscatter Diffraction (EBSD) analysis were polished with colloidal
silica before being carbon coated. Data were acquired on a NordlysNano and a NordlysMax EBSD detector (Oxford
Instruments). Working conditions during acquisition of the EBSD patterns were 20 kV, 20 mm working distance, 70° sample
tilt and high vacuum. AZtec software was used for pattern indexing on rectangular grids with step size of 0.7 µm, 1 µm and
1.8 µm. EBSD patterns were processed with the Channel 5 software (Oxford Instruments), and noise reduction was performed
170 following the procedure suggested in Bestmann and Prior (2003). The EBSD data are presented as grain size maps, with a 10°
misorientation threshold to define grain boundaries (in black), while low-angle boundaries are defined as having misorientation
> 2° and < 10° and are displayed as white or cyan lines. The grain size was measured as the diameter of a circle with equivalent
area to the grain. The spread of the internal orientation of each grain was shown as Grain Orientation Spread (GOS) maps and
was considered as a measure of the internal strain of the grain. A trade-off curve was used to calculate a threshold GOS value,
175 which separates recrystallized grains from relict grains, following the procedure outlined in Cross et al. (2017). The average
recrystallized grain size, calculated as root mean square (RMS), was used to apply the EBSD calibrated recrystallized grain
size piezometer for quartz (Cross et al., 2017). Grain reference orientation deviation angle maps (GROD) were used to visualise
subgrains only partially outlined by low-angle boundaries and to estimate their size. GROD maps are colour coded to show
the angular deviation at each point of a grain from the average orientation of the grain. Quartz c-axis orientation is presented
180 as pole figures on equal area, lower hemisphere projections, and one point per grain. The XY plane of the pole figure is parallel
to the shear zone foliation, X is parallel to the stretching lineation, and Z is normal to the foliation.

3.2 Mineral chemistry and Raman spectroscopy

A first semi-quantitative chemical composition point analysis was conducted using a JEOL 7001 FEG-SEM equipped with
energy-dispersive spectrometer (EDS) at the Electron Microscopy Centre of the University of Plymouth. Major element
185 mineral chemistry of chlorite and white mica was measured with Electron Microprobe Analysis (EMPA), at the Department
of Earth Sciences, University of Milan, Italy. Carbon coated thin sections were probed with a JEOL 8200 Super Probe equipped
with 5 wavelength-dispersive spectrometer (WDS). Working conditions were set to 15 kV of probe current, 5nA current on
sample, 1 µm beam diameter. Natural minerals were used for standardization, measurement times were 30s on peaks and 10s
on backgrounds of the X-ray lines.

190 Raman spectroscopy was applied for feldspar and opaque phase identification and for carbonaceous material (CM) characterization. Data acquisition was conducted at the Department of Chemistry, University of Padua (Italy), using a Thermo Scientific DXR MicroRaman spectrometer, equipped with a 532 nm depolarised laser. Spectra were acquired from polished thin section, using a laser power of 5 mW, spectrograph aperture 25 μm pinhole, and a 50X low distance objective. The estimate spot size was 1.1 μm in diameter and spectral resolution of 4.4 cm-1, with acquisition time of 30–90s. Feldspars composition

195 was classified on the basis of the acquired Raman spectra, as suggested in Freeman et al. (2008), using a comparison with standard Raman spectra from the RRUFF Project database (Lafuente et al. 2015). To assure a good statistical analysis of the CM structural heterogeneity, only samples with > 10 CM spectra were taken in consideration. Omnic software (Thermo Fisher Scientific) was used for Raman spectrum decomposition, using the software Lorentian/Gaussian function, following the procedure described in Koeketsu et al. (2009). A linear relationship between temperature and the Raman parameter R2 (derived

200 from the area of the defect band relative to the ordered graphite band) forms the basis of the CM geothermometer (Beyssac et al., 2002). Temperature can be estimated to ± 50 °C in the range 330–650 °C. Deformation can affect the internal disorder and underestimate the temperature obtained from the spectra analysis (Kirilova et al., 2017). To consider the possible role of deformation, analysis of CM both in the host rock and along the D_4 mylonitic foliation were collected. Care was taken to avoid CM within cracks, and to prevent altered measurement from CM damaged during the thin section polishing, we performed

205 measurements by focusing the laser beam on CM beneath the surface of a transparent adjacent grain as suggested in Beyssac et al. (2002).

4 Results

4.1 BFZ045 fault zone structure

Underground field observations and measurements indicate that BFZ045 is a strike-slip fault, with an average orientation of

210 87/095 (dip/dip direction, Fig. 2b) and with a mixed ductile-brittle deformation style that manifests itself as a 10-100 cm wide mylonite with a sinistral sense of shear, overprinted by cataclasites, fault breccias cemented by quartz, chlorite and sulphides, and by a network of veins typically filled with chlorite, quartz, and calcite. Slickensides with chlorite mineral striations are abundant throughout BFZ045 and the average orientation of the striations is 07/169 (plunge/trend, Fig. 2c). Stepped slickensides indicate a dominant sinistral sense of shear, although striations associated with dextral kinematics have also been

215 observed. The damage zone is typically 0-5 m thick and is characterized by an increased fracture density towards the fault core. Fractures are mostly filled by chlorite (Aaltonen et al, 2016).

The structure and the fault rocks of BFZ045 were characterized in detail from the two cores PH28 and PH16, both drilled approximately at the depth of 420 meters. The horizontal drill core PH28 provides a cross section of BFZ045, where a 2 m thick damage zone surrounds a 60 cm thick fault core characterised by a sub-vertical network of cohesive cataclasites and

220 veins that overprint a mylonite oriented 61/075 (dip/dip direction, Figs. 2a, b, d). A schematic representation of the fault

geometry along PH28 is represented in Fig. 2a. The host rock is a coarse-grained veined migmatite consisting of 40 vol% of quartz, 50 vol% of feldspars, and 10 vol% of muscovite (Fig. 2d, I).

The damage zone of BFZ045 consists of an asymmetrical (~20 cm east side of the core and ~ 60 cm on the west side) fractured host rock surrounding a mylonitic fault core (Fig 2a). Its boundaries were defined by the farthest occurrence of chlorite filled

225 fractures, identified microscopically as deformation band as they are associated with visible slip. A total of 12 fractures longer than 5 cm were observed along the core, of which 7 within a distance of 10 cm from the fault core (west side of the core). Fracture density increases towards the contact with the brittle fault core, with the average spacing between fractures decreasing from 3 cm to ca. 0.5 cm. Chlorite and calcite are the most common minerals partially filling the fractures oriented variably with respect to the mylonitic foliation. The contact between the damage zone and the mylonite is sharp.

230 The millimetre-spaced mylonitic foliation is defined by a compositional layering of alternating quartz-feldspathic domains and mica-rich domains (Fig. 2b, II). Rodding of quartz and feldspar defines a stretching lineation, with average orientation of 10/168 (plunge/trend) (Fig. 2b,c). Multiple slip surfaces marked by 0.5 – 10 cm thick cataclastic domains overprint the mylonite along the foliation (Fig. 2d, III). Locally, phyllosilicates and trails of opaque minerals define thin (<1mm thick) anastomosing foliation planes within the cataclasites, which wrap around sub-angular fragments of the mylonitic precursor.

235 Along a thin (<5 mm thick) slip surface, two pseudotachylyte injection veins intruding the mylonite at a high angle have been observed, which demonstrates the transient seismogenic behaviour of BFZ045. The pseudotachylyte main generation surface is less than 1 mm thick and is parallel to the mylonitic foliation (Fig. 3c). Calcite veins (1-3 mm thick) overprint the fault core either at high angle to the foliation or along the slip surfaces. Representative micrographs of samples taken from the fault core and from its damage zone are shown in figure 3.

240 **4.2 Microstructures and petrography**

The migmatitic host rock mineral assemblage observed in the PH28 samples consists of 50 % of quartz (qtz), 40 % K-feldspar (kf), and plagioclase (pl) and the remaining 10% of white mica (wm), alteration minerals of plagioclase (sericite) and secondary chlorite and calcite veins. Coarse-grained (1-2mm) quartz and feldspars are homogeneously distributed in an equigranular texture and show mostly straight grain boundaries. K-feldspar occurs as orthoclase, with a well-developed veined perthitic texture. Plagioclase, albitic in composition as determined from Raman analysis, has lamellar twinning and is commonly altered into sericite. Both types of feldspar locally show bent twin lamellae and undulose extinction. White mica was observed occasionally as millimetric sub-euhedral grains.

The damage zone retains the same mineral assemblage of the host rock, except along the chlorite filled shear bands and fractures (Fig 3a). Shear bands appear as cohesive micro-cataclasites, with fine grained (< 10 µm) chlorite surrounding angular

250 feldspar and quartz clasts. Calcite veins are preferentially oriented at high angle to the mylonitic foliation (60° to 85°). Microfractures in feldspars are preferentially oriented parallel and at low angle (≤ 20°) to the foliation. Both orientations correspond to the orientation of fluid inclusion trails observed in quartz (section 4.3.1).

Solid Earth
Discussions

Open Access

EGU

The relative mineral abundances in the mylonite are slightly different from those in the host rock, and consist of 50% quartz, 20% white mica + chlorite, and 30% K-feldspar + plagioclase. Accessory phases are rutile, anatase, and apatite, which are

255 typically found associated with chlorite to form black seams. The spaced mylonitic foliation is defined by a compositional banding between alternating millimetre-thick quartz bands and narrower (0.2 to 1 mm thick) mica- and feldspars-rich bands (Fig. 3b). Porphyroclasts of K-feldspar are up to 7 mm in size and show asymmetric pressure shadows filled with chlorite + muscovite ± feldspars (albite and K-feldspar), with a geometry indicative of a sinistral sense of shear. Veins of radiate chlorite are observed cutting the mylonitic foliation at a high angle (~60°).

260 The brittle overprint in the fault core occurs mostly as 3 to 10 cm thick protocataclasites, with chlorite rich C' shear bands cutting the mylonitic foliation and indicative of a sinistral sense of shears. The protocataclasite transitions to 0.5 - 2 cm thick cataclasite bands in the fault core. Compared to the host rock the cataclasite bands are richer in chlorite and opaque minerals, which occur as fine-grained (2-10 µm) flaky aggregates within the quartz + feldspars + muscovite rich matrix. Clasts are predominantly angular fragments of the mylonite, ranging in size from 100 µm to 5 mm, and surrounded by a variable

265 proportion of fine grained (<50 µm) matrix (Fig. 3c). Foliation in the matrix is defined by aligned phyllosilicates and anastomosing dark seams of opaque minerals. Veins with radiate chlorite that typically overprint the mylonite were also observed within mylonitic clasts inside the cataclasite.

A fine grained pseudotachylyte generation surface is observed subparallel to a cataclastic band (Fig. 3c), identified from characteristic centimetric injection veins, branching in the mylonitic rock at high angle to the foliation. The matrix of the

270 pseudotachylyte is completely altered to a fine-grained, <2 µm, chlorite and muscovite rich matrix that surrounds survivor clasts of quartz and rutile (Fig. 3d).

In the following section, we present a detailed description of quartz deformation and recrystallisation microstructures in the mylonite and in the cataclasite. We used the varying deformation microstructure of quartz as a proxy for the variation of differential stress and fluid pressure during the deformation of BFZ045 at the brittle-ductile transition.

275 **4.3 Quartz microstructures**

4.3.1 Damage zone

The damaged host rock shows large sub-euhedral quartz grains (> 3mm) with lobate to straight grain boundaries. Quartz displays intracrystalline deformation features such as undulatory extinction, wide extinction bands (WEBs, following the terminology of Derez et al., 2015; Fig. 4a), and bulges resulting in sutured grain boundaries (Fig. 4b; Stipp and Kunze, 2008).

280 WEBs are locally bounded by fluid inclusion trails with different orientations, which give them a blocky or slightly elongated aspect (Figs. 4a-b). Two main sets of intracrystalline fluid inclusion trails are observed, one at a low angle with respect to the mylonitic foliation and the other perpendicular to the foliation. Fine bulges (10-20 µm in size) occur along grain boundaries and intercrystalline fractures (Fig. 4a). Quartz grains in the proximity of the mylonite (sample PH28-2, Fig. 2b) develop intracrystalline bands of recrystallized grains sub- parallel to the foliation, with grain size of ~ 30-60 µm.

4.3.2 Fault core

285   Quartz in the mylonite presents various degrees of recrystallization (Figs. 5a-c). In zones where ductile deformation is less prominent (e.g. samples PH28_3, PH16_1, Fig. 2), quartz retains a coarser grain size (1-5 mm), and forms slightly asymmetric (sigmoidal-shaped) grains. Internally, the grains display patchy undulatory extinction, well-developed blocky to elongated WEBs (100-300 μm wide), and discrete intracrystalline bands (< 200 μm wide) of bulges and recrystallized grains

290   preferentially oriented sub-parallel to the foliation and at ca. 45° from the foliation, measured clockwise (Fig. 5a). The host grains contain small subgrains (< 60μm), which, towards the boundaries of the host grain, make transition to aggregates of recrystallized grains of size comparable to the subgrains, forming typical core-and-mantle microstructures (Fig. 5a).

    In zones of complete recrystallization at a distance >2 cm from the cataclastic fault zone core, quartz forms highly elongated polycrystalline ribbons (up to 0.5 – 1 mm thick, and up to 2 cm long) parallel to the foliation (Fig. 5b). The recrystallized

295   grains locally define a shape preferred orientation (SPO in Fig. 5b) inclined with 10° to 30° with respect to the trace of the foliation, consistently with the bulk sinistral sense of shear.

    Adjacent to the cataclastic unit, at a distance < 1 cm (sample PH16_3, Fig. 2), ataxial/unitaxial (i.e. with no visible median line; Bons, 2012) quartz veins are observed (Fig. 5c). They occur parallel to the mylonitic foliation (and to the layers of recrystallized quartz) and contain grains elongated normal to the vein boundary (i.e. normal to the foliation). The vein crystals

300   range in length from 200-400 μm and have a maximum thickness of 150 μm measured parallel to the vein. Quartz in the veins shows undulatory extinction and bulges at the grain boundaries (Fig. 5d) indicative of crystal plastic deformation. The recrystallized quartz in the mylonite surrounding the vein has a finer grain size than the one in the mylonite described in Figs. 5a-b, which is located farther away from the cataclastic core.

305   Quartz in the mylonite at distances < 2 cm from the cataclasites occurs in almost entirely recrystallized ribbons with a finer grain size (ca. 10 μm) than the one observed at higher distances from the brittle fault core (Fig. 5e). The quartz clasts in the cataclasite (Fig. 5f) preserve the deformation and recrystallization microstructures observed in the mylonite in close proximity to the cataclasite (Fig. 5e).

4.4 EBSD and grain size analysis of quartz

310   **4.4.1 Mylonite**

    EBSD analysis of the mylonite was conducted on sample PH16_1, which is located at the mylonitic shear zone boundary at a distance of 4 cm from the brittle fault core (Fig. 2a). EBSD maps were acquired from intracrystalline bands of recrystallized grains within an elongated mm- sized quartz grain (Fig. 6a), and from a highly recrystallized quartz layer along the mylonitic foliation (Fig. 7a).

315   The recrystallized grain size within the intracrystalline bands ranges from 5 to 60 μm (Fig. 6b, c). The Grain Orientation Spread (GOS) within the recrystallized bands varies between 0° and 8.4°, with a threshold value of 1° between the recrystallized grains

and the relict grains when analysing the trade-off curve proposed by Cross et al. (2017). The average grain size of recrystallized grains (GOS < 1°) is 16 ± 7 μm whereas relict grains (GOS > 1°) have an average grain size of 25 ± 9 μm. Relict grains contain subgrains of an average size of 17 ± 7 μm (Fig. 6f).

320   Quartz grain hosting the intracrystalline band shows subgrains of approximately 25-50 μm in size, which is comparable to the size of the coarser recrystallized grains observed in the intracrystalline bands (Fig. 6c). The size of the subgrains in the host quartz was estimated visually with the aid of Grain Relative Orientation Distribution maps (GROD, Fig. 6g).

In the recrystallized quartz layer (Fig. 7a), quartz grain shape ranges from equant to elongate parallel to the foliation, with grain size ranging from 5 to 87 μm (Figs. 7b, c). Grain Orientation Spread (GOS analysis identified a threshold value of 1.56°

325   to separate recrystallized- and relict grains (Fig. 7d). Average grain size of the recrystallized grains is 18 ± 8 μm, while relict grains have an average size of 28 ± 11 μm (Fig. 7e).

The relict grains contain subgrains of an average size of 17 ± 7 μm (Figs. 7c, f). The crystallographic preferred orientation (CPO) of the c-axis of the relict grains and recrystallized grains forms a single girdle consistently inclined with the sinistral sense of shear of the sample (Fig. 7g). The EBSD-calibrated recrystallized grain size piezometer for quartz of Cross et al.

330   (2017) was used to estimate the differential stresses during plastic flow in the mylonite. The estimated differential stress is 73-80 MPa for the average recrystallized grain size of 16-18 μm.

4.4.2 Vein parallel to the mylonitic foliation

The quartz vein parallel to the foliation shown in Fig. 5c and 8a was analysed to identify possible evidence of crystal-plastic deformation and dynamic recrystallization. Grain shape varies from fibrous with elongation perpendicular to the vein wall, to

335   more equant/less elongate. Grain boundaries of vein crystals are straight to lobate, the latter most commonly observed in association with fine recrystallized grains and bulges (<15 μm in size) (Figs. 8 b, c). Irrespective of their shape, most of the grains contain low-angle boundaries and Dauphiné twins. The low-angle boundaries are typically arranged to define polygonal to slightly elongated domains of ~10 μm in size, comparable to that of the surrounding recrystallized grains in the mylonite (Fig 8c).

340   Quartz in the mylonite flanking the vein shows fine grain size (<20 μm), with only a small fraction of coarser grains (30-60 μm). Grain Orientation Spread (GOS) analysis indicates that dynamic recrystallization is pervasive. The mean recrystallized grain size is 10 ± 3 μm, and the relict average grain size is 20 ± 9 μm, with a GOS threshold value of 1.94° (Figs. 8d, e). Selected relict grains (size> 40 μm) in the mylonite contain subgrains with size between 5 to 25 μm range (Fig. 8f). Finer grains observed within the vein also present a GOS value below the threshold, which suggests they represent the recrystallized

345   fraction in the quartz vein (Figs. 8c, f). In the vein quartz, GOS analysis indicates that the average subgrain size is 24 ± 7 μm, although the largest fraction of subgrains is smaller than 15 μm, i.e., similar in size to the recrystallized grains in the flanking mylonite and in the vein itself. The c-axis CPO of the recrystallized grains in the mylonite forms a single girdle synthetically inclined with the sinistral sense of shear (Fig. 8h). The c-axis CPO of recrystallized grains in the veins overlaps with the one

of the relict grains (Fig. 8i). The differential stress estimated from the average recrystallized grain size in the mylonite (10 μm)
350 is 106 MPa.

4.4.3 Cataclasite

We analysed a largely recrystallized quartz clast in the cataclasite from sample PH28_10 (Fig. 9a). The selected clast is rotated
of less than 10° with respect to the adjacent mylonitic foliation. Quartz grain size in the clast ranges from 4 to 60 μm. The
coarser grains are elongated parallel to the foliation, show bulges and fine recrystallized grains at their boundaries, and contain
355 a high density of low-angle boundaries (Fig. 9b). The low-angle boundaries define small polygonal domains of a size
comparable to the one of the recrystallized grains found at the grain boundaries (Fig. 9c). The GOS map in figure 9d identifies
two grain size distributions, separated by a GOS threshold value of 3.23°. The recrystallized grains (average grain size: 8 ± 4
μm) form equigranular aggregates at the boundaries of the coarser (average grain size: 17 ± 10 μm) elongated relict grains.
The c-axis CPO of the recrystallized grains and of the relict grains is the same, showing two maxima at an intermediate position
360 between the centre of the pole figure and its periphery, and consistently inclined with the sinistral sense of shear of the sample
(Fig. 9f). The differential stress estimated from the average recrystallized grain size in the clast (8 μm) is 123 MPa. Although
the map has been acquired from a clast, these microstructures and recrystallized grain size are representative of the mylonite
in the immediate vicinity (< 2 cm) of the brittle fault core (Figs. 5e, f).

4.5. Mineral chemistry, Raman spectroscopy, and pressure-temperature (P-T) conditions of deformation

365 We estimated the P-T conditions of mylonitic and cataclastic deformation using Raman spectroscopy of carbonaceous material
(RSCM), chlorite thermometry, and phengite barometry. Carbonaceous material was observed as grains and aggregates
ranging in size from ~50 to ~200 μm in the host rock (sample PH21_1, Fig. 10a) and as smaller grains (20- 50 μm) along the
mylonitic foliation, (sample PH16_1-2, Fig. 10b) along chlorite and muscovite rich layers. We estimated a peak metamorphic
temperature of 530°± 50° for the carbonaceous material in the host rock (using the thermometer calibration for a laser
370 wavelength of 514 nm, Beyssac et al. 2002), and a lower T of 436° ± 50° for the mylonite (Aoya et al., 2010, using the
thermometer calibration for a laser wavelength of 532 nm) (Fig. 11a).

The average compositions of white mica are listed in Table 1. The full dataset of chemical compositions of white micas is
reported in the Supplementary Material (S1). White mica composition was measured for grains parallel to the foliation
associated with stable K-feldspar (Figs. 10c, d) and structural formulae were calculated assuming 11 oxygens. The range of Si
375 apfu in the probed muscovite grains is 3.12 –3.16. This compositional range indicates a pressure of 2-4 Kbar using the Si-in-
phengite geobarometer (Fig. 11b, Massonne and Schreyer, 1987), considering the average temperature of 440°C derived with
the graphite thermometry.

Chlorite composition was determined for i) chlorite grains intergrown with quartz and muscovite in the strain shadows around
feldspar porphyroclasts in the mylonite (Fig. 10c, d), ii) chlorites flakes aggregate in the cataclasite quartz matrix (Fig. 10e),
380 and iii) radiate chlorites filling veins at high angle to the mylonitic foliation (Fig. 10f). The structural formula of chlorite was

calculated based on 14 oxygens, and representative composition are shown in Table 2. The full dataset of chemical compositions for chlorite is reported in the Supplementary Material (S2).

Chlorites along the mylonitic foliation and in the cataclasite have similar Si content (2.54 - 2.75 apfu), Al between 2.48- 2.82 apfu, and are moderately Fe-rich with a XFe (XFe=Fe/(Fe+Mg)) between 0.62 and 0.82. Chlorites in the mylonitic sample
385   from PH_16 have a more narrow range of XFe, between 0.5 and 0.6. The radial chlorite filling the veins has Si content between 2.51 and 2.780 apfu, Al between 2.74 and 3.00 apfu, and smaller XFe variations, between 0.69 and 0.81. In general, BFZ045 chlorites have a aphrosiderite-ripidolite composition and the microprobe results show that the composition of distinct chlorite generations is similar (Fig. 11c). The CHL(2) semi-empirical thermometer of Lanari et al. (2014) was applied to each EMPA analysis of chlorite with Si<3 apfu and (Na + K + Ca) < 0.1apfu. FeO was used as Fe total, and aH2O=1 and aSiO2=1 were
390   assumed. The estimated temperature for the mylonite ranges from 380 °C to 500 °C (limit of the used thermometer), with an average T of 440 °C for an assumed P of 3.5 kbar (Fig. 11d). Mean temperatures estimated for the cataclasite matrix (414 °C) and for the radiated chlorite in the veins (424 °C) are slightly lower than those of the mylonite, and compositions yielding T lower than 400 °C are more frequent, especially in the cataclasite (Fig 11d). The estimated temperature varied by 10 °C every 0.5 kbar increment.

395   **5. Discussion**

Our observations constrain the details of the structure and the deformation history of BFZ045. In particular, the microstructures of fault rocks indicate a sequence of deformation events where ductile deformation (mylonitisation) was punctuated by brittle deformation (veining), and eventually culminated in the formation of the brittle, cataclastic fault core. We interpret this sequence to result from the evolving stress history and fluid pressure variations along the fault. In the following, we discuss
400   the constraints provided by our microstructural analysis, and derive a conceptual model of fault slip behaviour of BFZ045 at the brittle-ductile transition.

5.1 The sequence of deformation events in BFZ045: ductile-brittle deformation cycles in the middle crust

Our microstructural observations are consistent with the general conclusion that brittle deformation along BFZ045 exploited
405   a ductile (mylonitic) precursor (Nordbäck and Mattila al., 2018; Skytta and Torvela, 2018). Veins, cataclasites and pseudotachylytes are localised along the mylonitic fabric of BFZ045, and only minor evidence of brittle deformation (mostly in the form of fractures filled by chlorite) is present outside of the mylonitic fault core (Figs. 2a, 3a). The analysed samples document a switch from dominant ductile to brittle deformation mode, via a transitional deformation stage where overall ductile conditions were punctuated by veining.
410   The first stage of deformation of BFZ045 is represented by the development of a localized N-S trending mylonitic foliation in the migmatites (Figs. 2, 3b, 5a, 5b). Mylonitic creep was punctuated by transient brittle events, with the opening of extensional

fractures along the mylonitic foliation filled by quartz veins (Figs. 5c, d). Veining was again followed by mylonitic deformation, as indicated by dislocation creep and dynamic recrystallization microstructures of quartz in the veins. Mylonite and veins were then overprinted by brittle deformation that formed cm- thick cataclasites (Figs. 3c, 5e, 5f) and a <0.5 cm thick

415 pseudotachylyte that, together, form the brittle fault core of BFZ045. The pseudotachylyte is recognizable from injection vein intruding the mylonitic precursor (Fig. 3c,d).

The parallelism between stretching lineation in the mylonite and chlorite slickenlines in the cataclasites indicates that the ductile-brittle deformation history of BFZ045 occurred under a constant strike-slip regime with sinistral kinematics, as shown by the kinematic indicators in the mylonites and by the stepped slickensides observed in the field. This conclusion is consistent

420 with the model of the brittle evolution of SW Finland proposed by Mattila and Viola (2014), which attributes the sinistral kinematics of NNW-SSE trending subvertical faults to the ductile-brittle transition stage of the basement at 1.75 Ga (stage 1 of deformation in Mattila and Viola, 2014). BFZ045 experienced later reactivations during the prolonged brittle history of the SW Finland basement, as indicated by calcite veins cutting the brittle fault core and by (rare) slickenlines with dextral kinematics observed in the underground exposures (Aaltonen et al. 2016). Local dextral kinematics along BFZ045 is

425 potentially consistent with the stage 2 of deformation of Mattila and Viola (2014) at 1.7-1.6 Ga. These later features, however, are not discussed further in this paper as they are subordinate to, and did not obliterate the earlier history.

The sequence of deformation events recorded along BFZ045 is estimated to have occurred in the middle crust under slightly decreasing T from 450-500 °C to 320-400 °C (Fig. 11). We note that cataclasites and pseudotachylytes are not overprinted by mylonitic creep, which might indicate that they formed when the temperature was sufficiently low to favour predominantly

430 brittle deformation along BFZ045.

A temperature of 440 ± 50 °C is derived from graphite thermometry along the mylonitic foliation, which is approximately 100° degrees lower than the T of 530 ± 50 °C estimated from the graphite thermometry in the host rock fabric (Fig. 11a). This is consistent with the retrograded greenschist facies conditions attributed to the final stages of D_4 deformation in the SW Finland basement at 1.81-1.77 Ga (Lahtinen et al., 2005; Mänttäri et al., 2010). If the graphite analysed in BFZ045 represents

435 carbonaceous material that was mobilized after the D_2-D_3 deformation phases that formed the main foliation in the host rock, then the T of 440 ± 50 °C indicates the T of graphite crystallization during the D_4 greenschist facies metamorphic overprint and mylonitization of BFZ045. However, the difference in temperature between the host rock fabric and the shear zone can also be explained as the result of strain-induced disorder in the crystal lattice of the analysed graphite, which might result in an underestimation of the temperature of formation of the graphite (Kirilova et al., 2018). Considering the 50° error range of

440 the thermometer and the difference in estimate due to the use of two different calibrations that for the same R2 values can determine different temperatures (Fig. 12c) (Beyssac et al. 2002; Aoya et al. 2010), a temperature estimate of 440 ± 50 °C for the mylonite is acceptable.

A T of 440° was considered to constrain the P at the time of deformation along BFZ045 using the phengite geobarometer (Massonne et al, 1987) (Fig. 12d). The peak metamorphic temperatures obtained from the mylonite suggest a P of 3-4 kbar,

445 which overlaps with the P estimates based on stable mineral assemblages of Tuisku et al. (2010) of 3.7 – 4.2 kbar at the

culmination of regional metamorphism in Olkiluoto (phase D_2-D_3). We interpret this result as representative of the conditions during mylonitic deformation along BFZ045 in the middle crust after peak metamorphism.

Our estimate of P-T conditions of mylonitization of BFZ045 (~450 °C, 3-3.5 kbar) are consistent with the late Svecofennian orogeny and the emplacement and cooling of pegmatitic granites in SW Finland (Aaltonen et al. 2010). The pegmatitic granites

450   emplaced at 15-12 km depth, were then affected by the last stage of ductile deformation D_4 and cooled below 300 °C ca. 1.75 Ga ago (Aaltonen et al. 2010).

Our results indicate that the T ranges derived from chlorite thermometry in the mylonite and in veins cutting the mylonitic foliation overlap (Fig. 12d), with only a few analyses in the veins yielding T < 400°C. This overlap suggests that chlorite veining occurred early in the deformation history of BFZ045 (i.e. at T ≥ 450°C) and that it continued during decreasing T.

455   Constraining the T of formation of cataclasites is more difficult, because the chlorite grains might be fragments of the mylonitic chlorite. However, we only probed flake chlorite aggregate comparable to radiated chlorite in the cataclasite and we consider the radiate morphology as indicative of growth within the cataclasite (Fig. 10e). Thus, although we cannot rule out that a few of the probed grains were fragments, our results indicate that the cataclasite formed at T ≥ 320 °C and potentially as high as 450-500 °C. The lowest T estimate from chlorite thermometry (300-320 °C) is derived from a few grains in the cataclasite and

460   in the vein (Fig. 11d), and still locates the observed deformation activity in the middle crust at T ≥ 300°C. This is consistent with the results of Marchesini et al. (2019), who estimated a minimum T of 350°C for the early stages of deformation and emplacement of quartz veins along the dextral fault zone BFZ300 (conjugate to BFZ045). Considering an average P of 3.5 kbar during ductile-brittle deformation along BFZ045 and an average crustal density of 2.7 g/cm3, the depth of deformation corresponds to approximately 13 km, which is consistent with the depth typically considered as representative of the base of

465   the seismogenic crust at the BDTZ (e.g. Scholz, 1990, Kohlstedt et al., 1995). We note that our P estimate is valid only for the mylonitic creep stage of the deformation history of BFZ045, as no suitable geobarometer was found in the cataclasite.

5.2 Interpretation of quartz microstructures: stress history during mylonitic creep of BFZ045

Microstructural observations show that quartz in the BFZ045 mylonitic core accommodated deformation by dislocation creep. The most common recrystallization microstructures (bulges at the grain boundaries and within intracrystalline bands, and core

470   and mantle microstructures with subgrains of comparable size to that of the recrystallized grains: Figs. 4, 5) suggest that bulging and subgrain rotation were the dominant recrystallization mechanisms (Hirth and Tullis, 1992; Stipp and Kunze, 2008). The average recrystallized grain size in all our samples falls within the range where bulging, defined as slow grain boundary migration coupled to localised subgrain rotation at the mantle of the host grain, is expected to be the dominant recrystallization mechanism (Stipp et al., 2010). Our microstructural observations and EBSD maps are consistent with this.

475   The average recrystallized grain size of quartz decreases from the mylonitic shear zone boundary (16-18 μm) towards to shear zones centre (8-12 μm), which has been overprinted by the brittle fault zone core (Fig. 12). In all the areas investigated with EBSD, we regularly observed two populations of grains in which the coarser (relict) grain size contains subgrains of size comparable to the average grain size of the finer recrystallized grains (Figs. 7-10). The CPO of relict and recrystallized grains

is the same, and this is consistent with the host-controlled development of a CPO during subgrain rotation recrystallization

480   (e.g. Stünitz et al. 2003). Despite the slight differences in CPO patterns between the individual analysed sites (Figs. 8-10), the key observation is that the CPO of both the coarse (16-18 μm in samples PH16_1) and the fine (8-12 μm in samples PH16_3 and PH28_10) recrystallized grain size fraction is consistently inclined with the sinistral sense of shear of the samples. We interpret the consistent sinistral asymmetry of the quartz c-axis CPOs as strong evidence that the different recrystallized grain size fractions all developed during sinistral strike-slip ductile activity of BFZ045. Thus, the grain size variations, and in

485   particular the fine recrystallized grain size observed in samples PH16_3 and PH28_10, are interpreted to result from the stress history during mylonitic deformation of BFZ045, and not from discrete events of late reactivation and overprint of the fabric. We interpret the recrystallized grain size of 16-18 μm as representative of the long term 'steady state' mylonitic flow of BFZ045 at a differential stress of 73-80 MPa. Such grain size is the most representative of the partially- (Fig. 7) and of the nearly completely (Fig. 8) recrystallized quartz ribbons in the BFZ045 mylonite at distances ≥ 4 cm from the brittle fault core,

490   and occurs as relict grain size in quartz clasts embedded in the cataclasite, where it is overprinted by finer recrystallized grains (Fig. 10). It is worth noting that quartz in the mylonite in close proximity to the cataclasite, as well as in clasts within the cataclastite (samples PH28_7-10 and PH16_3 in Fig. 2), systematically exhibits a large number of recrystallized grains belonging to the finer population (8-12 μm, Figs. 9, 10). This overprint is interpreted as the evidence of a local increase in stress (up to 120 MPa) during mylonitic creep (Kidder et al. 2016). The average recrystallized grain size of 16-18 μm is

495   associated with relict grains of 25-28 μm (Figs. 7-8), and un-recrystallized portions of quartz contain subgrains of similar size (≥ 25 μm, Figs. 7b-d). We speculate that the 25-28 μm grain size population might represent an early, lower stress (i.e. around 50-60 MPa) dynamic recrystallization event within BFZ045, which was later overprinted by recrystallization occurring under progressively increasing differential stress.

Our discussion of the stress history of BFZ045 relies on the GOS method to separate between relict and recrystallized grains.

500   It is known that the GOS method has a slight grain size bias, which results in higher GOS values for larger grains (Cross et al., 2017). However, this bias has no impact on the ability to separate between relict and recrystallized grains where their size overlaps on the cumulative grain size distribution, and the GOS-based separation is considered robust (Cross et al., 2017). One key observation that supports our GOS-based separation is that relict grains systematically contain subgrains of the same size of the new, finer recrystallized grains. Thus, we are confident that our analysis has reliably identified different recrystallized

505   grain sizes.

In summary, the differential stresses estimated from the different populations of recrystallized quartz grains increase from 73-80 MPa to a peak value of 120 MPa towards the contact with the cataclasite. An earlier, lower stress (ca.54 MPa) deformation is possibly recorded in the (few) relict quartz grains of 25-28 μm that contain subgrains of around 17 μm of average size (Figs. 7, 8). We are aware of the uncertainties and limitations of the palaeopiezometric calibrations, and our estimated flow stresses

510   must be taken with care. However, we consider the systematic decrease in recrystallised grain size towards the cataclastic fault core to be meaningful and to reflect a change in the rheological conditions during mylonitic creep. Given the similar T

conditions across the studied profile, we conclude that this change reflects an increase in stress and strain rate. To explain this increase in stress and strain rate towards the shear zone centre, we discuss two possibilities:

(1) Increasing stress and strain rate towards the brittle shear zone centre may reflect the rheological evolution of a shear zone

515   that is narrowing with progressive exhumation from the ductile to the brittle crust. In such a model, the peak stress conditions are reached at the brittle-ductile transition under progressively decreasing T (e.g. Kohlstedt et al., 1995; Behr and Platt, 2011). The results of our chlorite thermometry study support this model, as they are consistent with an overall T decrease from 450-500 °C to 320 °C during protracted mylonitic creep followed by a cataclastic overprint along the brittle fault core. In this scenario, BFZ045 would represent a case of narrowing shear zone that evolved from a distributed- to a progressively more

520   localised ductile deformation and eventually brittle deformation during cooling and exhumation (type II shear zone of Fossen, 2017). During this evolution, dislocation creep and fluid-assisted veining occurred simultaneously, as expected in the 270-350° C temperature range considered typical of the frictional-viscous transition in quartz-rich rocks (Dunlap et al., 1997; Handy et al., 1999; Stöckhert et al., 1999; Stipp et al., 2002). Our work is unable to constrain the amount of exhumation associated with the cooling and progressive localization in the brittle fault core, as the strike-slip nature of BFZ045 cannot be

525   responsible of significant exhumation. Considering a transpressional regional tectonic regime during the sinistral strike-slip activity of BFZ045 (stage 1 of deformation in Mattila and Viola, 2014), we speculate that the combination between thrusting and erosion was the main exhumation process of the Olkiluoto basement at around 1.75 Ga. In this scenario, BFZ045 was active within the Olkiluoto basement while it was being passively exhumed. However, we emphasize that a detailed appraisal of the mechanisms responsible of the passive exhumation of the Olkiluoto basement is beyond the scope of this study. Kärki

530   and Paulamäki (2006) estimated a regional geothermal gradient of ca. 40 °C km^{-1} during retrogressive metamorphic conditions that culminated in the post-D_4 exhumation of the Olkiluoto basement. Assuming a regional geothermal gradient of ca. 40 °C km^{-1}, mylonitic deformation of BFZ045 at 440-500 °C would have occurred at ca. 11-12 km depth, whereas cataclastic deformation at 320-400 °C at 8-9 km depth.

(2) Alternatively, and assuming that the cataclasite formed at similar T (and depth) of the mylonite (T ≥ 400 °C), the increase

535   in stress recorded by the finer recrystallized grain size might be attributed to external stress loading from seismic faulting in the overlying upper crust (i.e. seismic loading) (e.g. Küster and Stöckhert, 1998; Trepmann and Stöckhert, 2003; Trepmann et al., 2017; Trepmann and Seybold, 2019). The presence of pseudotachylytes along the BFZ045 fault core indicates that the fault was capable of generating earthquakes, and the seismogenic behaviour of other faults in the Olkiluoto basement has been previously discussed (Marchesini et al., 2019 and refs. therein). Thus, local high differential stresses in the BFZ045 mylonites

540   could had been induced by seismic activity in the overlying upper crust. However, the fine-grained recrystallized fraction is exclusively localised in the immediate vicinity of the brittle fault core of BFZ045, whereas in case of earthquake-induced stress variations a more diffuse overprint within the entire width of the shear zone (and perhaps even outside of it) would be expected. Dislocation glide-controlled deformation microstructures of quartz typically interpreted as the evidence of seismic loading in the ductile crust, such as conjugate micro-shear zones, short wavelength undulatory extinction, and sub-basal deformation

545   lamellae (Trepmann and Stöckert, 2013; Trepmann et al., 2017) have not been observed in the mylonite and in the damage

zone of BFZ045 (Figs. 3-5). Furthermore, cataclasites and pseudotachylytes are not mylonitised, and this is consistent with overall decreasing temperature conditions that inhibited the efficiency of thermally activated creep processes. Thus, we favour the model whereby the documented decrease in the recrystallized grain size of quartz towards the BFZ045 fault core reflects the rheological evolution of a narrowing shear zone, which reached peak stress conditions at the BDTZ.

550 **5.3 Conceptual model of the fault slip behaviour of BFZ045 at the base of the seismogenic zone**

In order to estimate the relative contributions of variations in fluid pressure and differential stress in facilitating different fault slip behaviours, we modelled a possible failure mode evolution of BFZ045 using the λ-σ failure mode diagram (Cox, 2010), with the following assumptions and using the following parameters:

- We assumed a strike-slip Andersonian regime of faulting, according to the deformation history proposed by Mattila
555 and Viola (2014). This is consistent with the dominant strike-slip stretching lineations and slickenlines observed on the core samples. In a strike-slip regime, the vertical stress is σ2, which we assume to correspond to the lithostatic load during deformation. This was estimated at 300-350 MPa during mylonitic creep from the phengite barometer. The maximum differential stress during stage 1 and stage 2 was considered to be in the range between 55 and 60 MPa, whereas during stage 3 and stage 3 to stage 4 transition we consider a differential stress increasing progressively from 73 to 123 MPa. σ1 and σ3
560 values were calculated for a stress ratio R of 0.3 estimated by Mattila and Viola (2014) for the N-S sinistral faults in Olkiluoto. R is defined as R= σ2- σ3/ σ1- σ3

- Strain rate during mylonitic creep was calculated using the dislocation creep flow law of quartzite Eq. (1):

$$\dot{\varepsilon} = A\sigma^n f_{H2O}^m \exp(-Q/RT)$$

565 (1)

where $\dot{\varepsilon}$ is the strain rate, A an empirical constant, σ the differential stress, n the stress exponent, f_{H2O} the water fugacity, m the water fugacity exponent, Q the activation energy, R the gas constant, and T the temperature. Using the flow law for wet quartzite of Hirth et al. (2001), we estimated the following strain rates during mylonitic creep: $\dot{\varepsilon}$ = 4.3 x 10^{-13} s^{-1} (for a differential stress of 50 MPa during stage 1), $\dot{\varepsilon}$ = 1.1 x 10^{-12} s^{-1} (for a differential stress of 73-80 MPa at the beginning of stage
570 3), and $\dot{\varepsilon}$ =6.9 x 10^{-12} s^{-1} (for the peak stress conditions during stage 3). Water fugacity was calculated with Wither's fugacity calculator based on Pitzer and Sterner (1994) equation of state for 450º and 3.5 Kbar (water fugacity exponent m = 1 in Hirth et al., 2001).

- We assumed that viscous creep in the mylonite occurred at fluid pressure conditions higher than hydrostatic (λ=0.6),
575 based on the Pf > 210 MPa proposed by Marchesini et al. (2019) for brittle failure under overall ductile conditions of the conjugate fault BFZ300.

- Failure envelope for λ -σ failure mode diagrams were calculated using a friction coefficient λ of 0.6 (common value for granitoids, e.g. Sibson 1985), a cohesive strength of 26 MPa and a tensile strength of 13 MPa, which were taken from

580 tensile strength measurements of granitic gneisses of Olkiluoto (Aaltonen et al., 2010).

Figure 13 shows the resulting model: stage 1 to stage 3 are representative of the deformation under ductile conditions, while stage 4 represents the final transition to brittle deformation. Failure envelopes were calculated for progressively shallower depths (Figs. 13c, d) in order to account for the progressive exhumation discussed in section 5.2. BFZ045 was initially undergoing ductile deformation at differential stress < 60 MPa and a strain rate of ca. 10^{-13} s^{-1} (Fig. 13a, stage 1), developing

585 a 25-28 µm recrystallized fraction. According to the failure envelope, low differential stresses (<80MPa) are necessary for extensional- and hybrid fractures to occur, therefore the emplacement of the foliation-parallel veins (Fig. 13b, stage 2) must predate the development of the finest recrystallized fractions developed under peak values (ca. 120MPa) of differential stress. While the foliation-parallel veins are consistent with mode I opening mode due to hydrofracturing, the overall geometric stress conditions during ductile deformation of BFZ045 are expected to generate en-echelon vein systems oblique to the foliation.

590 Thus, a transient reorientation of the stress field in the fault zone must be invoked to explain the foliation-parallel veins during stage 2. A regional rotation of the stress field appears unlikely, given the constant orientation of the stretching lineation and slickenlines in the core samples, and the consistent asymmetry of the pre- and post-vein quartz c-axis CPO (Figs. 7-9).

Transient high fluid pressure reaching lithostatic values (λ = 1) during low-differential stress mylonitic creep was necessary to trigger a change in the deformation behaviour, with a switch from viscous creep to mode I fracturing along the mylonite

595 foliation resulting in the emplacement of quartz veins (Fig. 13b, stage 2). The average subgrain size within the vein quartz is 24 µm (although the larger fraction is represented by subgrains smaller than 15 µm), which is similar to the population of the coarser recrystallized grains in the mylonite (Fig. 7). This might indicate that the quartz vein emplaced during an overall low differential stress creep event, which was later overprinted by progressively higher stress deformation as indicated by the subgrains < 15 µm in size and by the average recrystallized grain size of 12 µm both inside the vein and in the surrounding

600 quartz-rich mylonite.

Veining was then followed by a drop in fluid pressure (e.g. Sibson, 1989, 1993; Cox 1995) and a switch back to mylonitic creep (Fig. 13c, stage 3) under progressively higher stress conditions in a narrowing shear zone during slight cooling and exhumation (Fig. 13c, stage 3). Peak stress conditions recorded in the recrystallized grain size of quartz were reached in a highly localized shear zone at the fault core and corresponded to ca. 120 MPa (peak stress and strain rate during stage 3, Fig.

605 13c). Cataclasites and pseudotachylytes overprinted this localised shear zone and formed the brittle fault core of BFZ045 (Fig. 13d, stage 4). In order to meet the brittle shear failure criterion, high values of pore fluid pressure (λ> 0.75) is required at the peak stress of ca. 120MPa, but we cannot rule out that shear failure occurred by a combination of increase in fluid pressure and differential stress after mylonitic creep had ceased (Fig. 13d). Any potential increase of stress beyond the ca. 120 MPa estimated from the 8 µm recrystallized grain size cannot be captured by our microstructural analysis. We must note that the

610 actual path of variation of pore fluid pressure from stage 2 to stage 4 is not known, and we have no control on the extent of

Solid Earth
Discussions
Open Access
EGU

drop of pore fluid pressure after stage 2 (i.e., we do not know the value of λ during stage 3 mylonitic creep and prior to cataclasite formation in stage 4).

In summary, we propose the following conceptual model for the deformation history and the fault slip behaviour of BFZ045 in the Olkiluoto metamorphic basement (Fig. 13):

615

1. Stage 1 is represented by long-term mylonitic creep along a N-S trending shear zone (Fig. 13a);

2. Mylonitic creep was punctuated by the emplacement of foliation-parallel quartz veins (formation of mode I fractures, stage 2; Fig.13b);

3. During stage 3, the mylonite and the veins were overprinted by viscous creep under increased differential stress towards
620 what is now the BFZ045 brittle fault core (Fig.13.c);

4. During stage 4, cataclastic deformation and local generation of pseudotachylytes along the mylonitic foliation overprinted all the pre-existing structures (Fig.13.d).

Conclusions

This study shows that deformation microstructures can be used to evaluate the stress history of a narrowing shear zone
625 deforming across the brittle-ductile transition in the continental crust, and to reconstruct the deformation history of fault zones that experienced cyclical brittle-ductile fault slips. The fault zone BFZ045 exploited a mylonitic precursor in the Paleoproterozoic basement in SW Finland, and records transient brittle deformation in the form of syn-kinematic quartz veins emplaced during ongoing mylonitic creep in response to transiently high fluid pressure. Mylonitic deformation continued after the vein emplacement, as evidenced by the dynamic recrystallization of the vein quartz. Mylonitic creep occurred under
630 progressively increasing differential stress localised towards the shear zone centre in an overall narrowing shear zone that was deforming under slightly decreasing T from 400-500° C to ≥ 320° C. Mylonitic deformation at the shear zone centre records peak stress conditions of around 120 MPa, and was followed by brittle deformation that generated cataclasites and minor pseudotachylytes in the fault core. The entire deformation history documented in this study occurred at the base of the seismogenic crust at an estimated depth range of 9-13 km.
635 The constraints derived from microstructural analysis shaped the proposed conceptual model of the evolution of BFZ045 slip behaviour, which highlights the important role of transiently sub-lithostatic fluid pressure in triggering vein emplacement during ongoing mylonitic deformation, as well as of the progressive increase in stress and strain rate during viscous creep towards peak conditions reached at the BDTZ in the Fennoscandian Shield. This study shows that microstructural study leading to the acquisition of independent constraints offers the potential to reconstruct in detail the evolutionary history of fault zones
640 that experienced a transition in deformation mode at the BDTZ. In addition to deriving a conceptual model of varying fault slip behaviours at the BDTZ, the methods and the results of this work complement and expand thorough site characterization studies of deep geological disposal facilities.

Solid Earth
Discussions

Open Access

EGU

Acknowledgements

References

Aaltonen, I., Lahti, M., Engström, J., Mattila, J., Paananen, M., Paulamäki, S., Gehör, S., Kärki, A., Ahokas, T., Torvela, T. and Front, K.: Geological Model of the Olkiluoto Site. Version 2.0., Posiva Working Report 2010-70, Posiva Oy, Eurajoki, 2010.

655 Aaltonen, I., Engström, J., Gehör, S., Kosunen, P. and Kärki, A.: Geology of Olkiluoto, Posiva Working Report 2016-16, Posiva Oy, Eurajoki, 2016.

Aoya, M., Kouketsu, Y., Endo, S., Shimizu, H., Mizukami, T., Nakamura, D. and Wallis, S.: Extending the applicability of the Raman carbonaceous-material geothermometer using data from contact metamorphic rocks, Journal of Metamorphic Geology, 28(9), 895–914, doi:10.1111/j.1525-1314.2010.00896.x, 2010.

660 Austrheim, H.: Fluid and deformation induced metamorphic processes around Moho beneath continent collision zones: Examples from the exposed root zone of the Caledonian mountain belt, W-Norway, Tectonophysics, 609, 620–635, doi:10.1016/j.tecto.2013.08.030, 2013.

Behr, W. M. and Platt, J. P.: A naturally constrained stress profile through the middle crust in an extensional terrane, Earth and Planetary Science Letters, 303(3), 181–192, doi:10.1016/j.epsl.2010.11.044, 2011.

665 Bestmann, M. and Prior, D. J.: Intragranular dynamic recrystallization in naturally deformed calcite marble: diffusion accommodated grain boundary sliding as a result of subgrain rotation recrystallization, Journal of Structural Geology, 25(10), 1597–1613, doi:10.1016/S0191-8141(03)00006-3, 2003.

Beyssac, O., Goffé, B., Chopin, C. and Rouzaud, J. N.: Raman spectra of carbonaceous material in metasediments: a new geothermometer, Journal of Metamorphic Geology, 20(9), 859–871, doi:10.1046/j.1525-1314.2002.00408.x, 2002.

670 Bons, P. D., Elburg, M. A. and Gomez-Rivas, E.: A review of the formation of tectonic veins and their microstructures, Journal of Structural Geology, 43, 33–62, doi:10.1016/j.jsg.2012.07.005, 2012.

Bos, B. and Spiers, C. J.: Frictional-viscous flow of phyllosilicate-bearing fault rock: Microphysical model and implications for crustal strength profiles, Journal of Geophysical Research: Solid Earth, 107(B2), ECV 1-1-ECV 1-13, doi:10.1029/2001JB000301, 2002.

675 Ceccato, A., Menegon, L., Pennacchioni, G. and Morales, L. F. G.: Myrmekite and strain weakening in granitoid mylonites, Solid Earth, 9(6), 1399–1419, doi:https://doi.org/10.5194/se-9-1399-2018, 2018.

Cox, S. F.: Faulting processes at high fluid pressures: An example of fault valve behavior from the Wattle Gully Fault, Victoria, Australia, Journal of Geophysical Research: Solid Earth, 100(B7), 12841–12859, doi:10.1029/95JB00915, 1995.

Cox, S. F.: Structural and isotopic constraints on fluid flow regimes and fluid pathways during upper crustal deformation: An

680 example from the Taemas area of the Lachlan Orogen, SE Australia, Journal of Geophysical Research: Solid Earth, 112(B8), doi:10.1029/2006JB004734, 2007.

Cox, S. F.: The application of failure mode diagrams for exploring the roles of fluid pressure and stress states in controlling styles of fracture-controlled permeability enhancement in faults and shear zones, Geofluids, doi:10.1111/j.1468-8123.2010.00281.x, 2010.

685 Cross, A. J., Prior, D. J., Stipp, M. and Kidder, S.: The recrystallized grain size piezometer for quartz: An EBSD-based calibration: EBSD-Based Quartz Grain Size Piezometer, Geophysical Research Letters, 44(13), 6667–6674, doi:10.1002/2017GL073836, 2017.

Derez, T., Pennock, G., Drury, M. and Sintubin, M.: Low-temperature intracrystalline deformation microstructures in quartz, Journal of Structural Geology, 71, 3–23, doi:10.1016/j.jsg.2014.07.015, 2015.

690 Dunlap, W. J., Hirth, G. and Teyssier, C.: Thermomechanical evolution of a ductile duplex, Tectonics, 16(6), 983–1000, doi:10.1029/97TC00614, 1997.

Fossen, H. and Cavalcante, G. C. G.: Shear zones – A review, Earth-Science Reviews, 171, 434–455, doi:10.1016/j.earscirev.2017.05.002, 2017.

Freeman, J. J., Wang, A., Kuebler, K. E., Jolliff, B. L. and Haskin, L. A.: Characterization of natural feldspars by Raman

695 spectroscopy for future planetary exploration, The Canadian Mineralogist, 46(6), 1477–1500, 2008.

Fusseis, F. and Handy, M. R.: Micromechanisms of shear zone propagation at the brittle–viscous transition, Journal of Structural Geology, 30(10), 1242–1253, doi:10.1016/j.jsg.2008.06.005, 2008.

Gueydan, F., Leroy, Y. M., Jolivet, L. and Agard, P.: Analysis of continental midcrustal strain localization induced by microfracturing and reaction-softening, Journal of Geophysical Research: Solid Earth, 108(B2), doi:10.1029/2001JB000611,

700 2003.

Handy, M. R. and Brun, J.-P.: Seismicity, structure and strength of the continental lithosphere, Earth and Planetary Science Letters, 223(3), 427–441, doi:10.1016/j.epsl.2004.04.021, 2004.

Handy, M. R., Franz, L., Heller, F., Janott, B. and Zurbriggen, R.: Multistage accretion and exhumation of the continental crust (Ivrea crustal section, Italy and Switzerland), Tectonics, 18(6), 1154–1177, doi:10.1029/1999TC900034, 1999.

705 Handy, M. R., Hirth, G. and Hovius, N.: Continental Fault Structure and Rheology from the Frictional-to-Viscous Transition Downward, in Tectonic Faults: Agents of Change on a Dynamic Earth, MITP. [online] Available from: https://ieeexplore.ieee.org/document/6285583 (Accessed 13 July 2019), 2007.

Hey, M. H.: A new review of the chlorites, Mineral. Mag. J. M. Soc., 224, 277–292, https://doi.org/10.1180/minmag.1954.030.224.01, 1954.

710 Hirth, G. and Beeler, N. M.: The role of fluid pressure on frictional behavior at the base of the seismogenic zone, Geology, 43(3), 223–226, doi:10.1130/G36361.1, 2015.

Hirth, G. and Tullis, J.: Dislocation creep regimes in quartz aggregates, Journal of Structural Geology, 14(2), 145–159, doi:10.1016/0191-8141(92)90053-Y, 1992.

Hirth, G. and Tullis, J.: The brittle-plastic transition in experimentally deformed quartz aggregates, Journal of Geophysical

715 Research: Solid Earth, 99(B6), 11731–11747, doi:10.1029/93JB02873, 1994.

Hirth, G., Teyssier, C. and Dunlap, J. W.: An evaluation of quartzite flow laws based on comparisons between experimentally and naturally deformed rocks, Int J Earth Sci, 90(1), 77–87, doi:10.1007/s005310000152, 2001.

Kärki, A. and Paulamäki, S.: Petrology of Olkiluoto, 2006.

Kidder, S., Hirth, G., Avouac, J.-P. and Behr, W.: The influence of stress history on the grain size and microstructure of

720 experimentally deformed quartzite, Journal of Structural Geology, 83, 194–206, doi:10.1016/j.jsg.2015.12.004, 2016.

Kirilova, M., Toy, V., Rooney, J. S., Giorgetti, C., Gordon, K. C., Collettini, C. and Takeshita, T.: Structural disorder of graphite and implications for graphite thermometry., Solid Earth, 9(1), 2018.

Kjøll, H. J., Viola, G., Menegon, L. and Sørensen, B. E.: Brittle–viscous deformation of vein quartz under fluid-rich lower greenschist facies conditions, Solid Earth, 6(2), 681–699, doi:https://doi.org/10.5194/se-6-681-2015, 2015.

725 Kohlstedt, D. L., Evans, B. and Mackwell, S. J.: Strength of the lithosphere: Constraints imposed by laboratory experiments, Journal of Geophysical Research: Solid Earth, 100(B9), 17587–17602, doi:10.1029/95JB01460, 1995.

Kouketsu, Y., Mizukami, T., Mori, H., Endo, S., Aoya, M., Hara, H., Nakamura, D. and Wallis, S.: A new approach to develop the Raman carbonaceous material geothermometer for low-grade metamorphism using peak width, Island Arc, 23(1), 33–50, doi:10.1111/iar.12057, 2014.

730 Kukkonen, I. T. and Lauri, L. S.: Modelling the thermal evolution of a collisional Precambrian orogen: High heat production migmatitic granites of southern Finland, Precambrian Research, 168(3), 233–246, doi:10.1016/j.precamres.2008.10.004, 2009.

Küster, M. and Stöckhert, B.: High differential stress and sublithostatic pore fluid pressure in the ductile regime — microstructural evidence for short-term post-seismic creep in the Sesia Zone, Western Alps, Tectonophysics, 303(1), 263–277, doi:10.1016/S0040-1951(98)00256-X, 1999.

735 Lafuente, B., Downs, R. T., Yang, H. and Stone, N.: The power of databases: the RRUFF project, in Highlights in mineralogical crystallography, pp. 1–29, Walter de Gruyter GmbH., 2016.

Lahtinen, R.: Crustal evolution of the Svecofennian and Karelian domains during 2.1 - 1.79 Ga: with special emphasis on the geochemistry and origin of 1.93 - 1.91 Ga gneissic tonalites and associated supracrustal rocks in the Rautalampi area, central Finland ; with 7 tables, Geologian Tutkimuskeskus, Espoo., 1994.

740 Lahtinen, R., Korja, A. and Nironen, M.: Chapter 11 Paleoproterozoic tectonic evolution, in Developments in Precambrian Geology, vol. 14, edited by M. Lehtinen, P. A. Nurmi, and O. T. Rämö, pp. 481–531, Elsevier., 2005.

Lanari, P., Wagner, T. and Vidal, O.: A thermodynamic model for di-trioctahedral chlorite from experimental and natural data in the system MgO–FeO–Al 2 O 3–SiO 2–H 2 O: applications to P–T sections and geothermometry, Contributions to Mineralogy and Petrology, 167(2), 968, 2014.

745 Mänttäri, I., Talikka, M., Paulamäki, S. and Mattila, J.: U-Pb ages for tonalitic gneiss, pegmatitic granite, and diabase dyke, Olkiluoto study site, Eurajoki, SW Finland, Posiva Oy., 2006.

Mänttäri, I., Engstroem, J., Lahaye, Y. and Pere, T.: U-Pb ages for PGR dykes, KFP, and adjacent older leucosomic PGRs from ONKALO underground research facility, Olkiluoto, Eurajoki, SW Finland, Posiva Oy., 2010.

Marchesini, B., Garofalo, P. S., Menegon, L., Mattila, J. and Viola, G.: Fluid-mediated, brittle–ductile deformation at 750 seismogenic depth – Part 1: Fluid record and deformation history of fault veins in a nuclear waste repository (Olkiluoto Island, Finland), Solid Earth, 10(3), 809–838, doi:https://doi.org/10.5194/se-10-809-2019, 2019.

Massonne, H.-J. and Schreyer, W.: Phengite geobarometry based on the limiting assemblage with K-feldspar, phlogopite, and quartz, Contributions to Mineralogy and Petrology, 96(2), 212–224, 1987.

Mattila, J. and Viola, G.: New constraints on 1.7 Gyr of brittle tectonic evolution in southwestern Finland derived from a 755 structural study at the site of a potential nuclear waste repository (Olkiluoto Island), Journal of Structural Geology, 67, 50–74, 2014.

Melosh, B. L., Rowe, C. D., Gerbi, C., Smit, L. and Macey, P.: Seismic cycle feedbacks in a mid-crustal shear zone, Journal of Structural Geology, 112, 95–111, doi:10.1016/j.jsg.2018.04.004, 2018.

Menegon, L., Pennacchioni, G., Malaspina, N., Harris, K. and Wood, E.: Earthquakes as Precursors of Ductile Shear Zones in 760 the Dry and Strong Lower Crust, Geochemistry, Geophysics, Geosystems, 18(12), 4356–4374, doi:10.1002/2017GC007189, 2017.

Nguyen, P. T., Harris, L. B., Powell, C. M. and Cox, S. F.: Fault-valve behaviour in optimally oriented shear zones: an example at the Revenge gold mine, Kambalda, Western Australia, Journal of Structural Geology, 20(12), 1625–1640, doi:10.1016/S0191-8141(98)00054-6, 1998.

765 Nironen, M.: The Svecofennian Orogen: a tectonic model, Precambrian Research, 86(1–2), 21–44, 1997.

Nordbäck, N. and Mattila, J.: Brittle Fault Systems of the ONKALO Underground Research Facility, 2018.

Pajunen, M., Airo, M., Elminen, T., Mänttäri, I., Niemelä, R., Vaarma, M., Wasenius, P. and Wennerström, M.: Tectonic evolution of the Svecofennian crust in southern Finland, Geological Survey of Finland, Special Paper, 47, 15–160, 2008.

Pennacchioni, G. and Mancktelow, N. S.: Nucleation and initial growth of a shear zone network within compositionally and

770   structurally heterogeneous granitoids under amphibolite facies conditions, Journal of Structural Geology, 29(11), 1757–1780, doi:10.1016/j.jsg.2007.06.002, 2007.

Pere, T.: Fault-related local phenomena in the bedrock of Olkiluoto with particular reference to fault zone OL-BFZ100, Posiva Oy., 2009.

Pfiffner, O. A.: Basement-involved thin-skinned and thick-skinned tectonics in the Alps, Geological Magazine, 153(5–6),

775   1085–1109, doi:10.1017/S0016756815001090, 2016.

Pitzer, K. S. and Sterner, S. M.: Equations of state valid continuously from zero to extreme pressures for H2O and CO2, J. Chem. Phys., 101(4), 3111–3116, doi:10.1063/1.467624, 1994.

Ranalli, G.: Rheology of the lithosphere in space and time, Geological Society, London, Special Publications, 121(1), 19–37, doi:10.1144/GSL.SP.1997.121.01.02, 1997.

780   Saintot, A., Stephens, M., Viola, G. and Nordgulen, Ø.: Brittle tectonic evolution and paleostress field reconstruction in the southwestern part of the Fennoscandian Shield, Forsmark, Sweden, Tectonics, 30(4), 2011.

Scholz, C.: The Mechanics of Earthquakes and Faulting, Cambridge University Press, Cambridge., 1990.

Scholz, C. H.: Earthquakes and friction laws, Nature, 391(6662), 37, doi:10.1038/34097, 1998.

Sibson, R. H.: Fault zone models, heat flow, and the depth distribution of earthquakes in the continental crust of the United

785   States, Bulletin of the Seismological Society of America, 72(1), 151–163, 1982.

Sibson, R. H.: A note on fault reactivation, Journal of Structural Geology, 7(6), 751–754, doi:10.1016/0191-8141(85)90150-6, 1985.

Sibson, R. H.: Earthquake faulting as a structural process, Journal of Structural Geology, 11(1), 1–14, doi:10.1016/0191-8141(89)90032-1, 1989.

790   Sibson, R. H.: Conditions for fault-valve behaviour, Geological Society, London, Special Publications, 54(1), 15–28, doi:10.1144/GSL.SP.1990.054.01.02, 1990.

Sibson, R. H.: Implications of fault-valve behaviour for rupture nucleation and recurrence, Tectonophysics, 211(1), 283–293, doi:10.1016/0040-1951(92)90065-E, 1992.

Sibson, R. H.: Load-strengthening versus load-weakening faulting, Journal of Structural Geology, 15(2), 123–128,

795   doi:10.1016/0191-8141(93)90090-W, 1993.

Sibson, R. H. and Rowland, J. V.: Stress, fluid pressure and structural permeability in seismogenic crust, North Island, New Zealand, Geophys J Int, 154(2), 584–594, doi:10.1046/j.1365-246X.2003.01965.x, 2003.

Skyttä, P. and Torvela, T.: Brittle reactivation of ductile precursor structures: The role of incomplete structural transposition at a nuclear waste disposal site, Olkiluoto, Finland, Journal of Structural Geology, 116, 253–259, 2018.

800   Stipp, M. and Kunze, K.: Dynamic recrystallization near the brittle-plastic transition in naturally and experimentally deformed quartz aggregates, Tectonophysics, 448(1), 77–97, doi:10.1016/j.tecto.2007.11.041, 2008.

Stipp, M. and Tullis, J.: The recrystallized grain size piezometer for quartz, Geophysical Research Letters, 30(21), doi:10.1029/2003GL018444, 2003.

805 Stipp, M., Stünitz, H., Heilbronner, R. and Schmid, S. M.: The eastern Tonale fault zone: a 'natural laboratory' for crystal plastic deformation of quartz over a temperature range from 250 to 700°C, Journal of Structural Geology, 24(12), 1861–1884, doi:10.1016/S0191-8141(02)00035-4, 2002.

Stipp, M., Tullis, J., Scherwath, M. and Behrmann, J. H.: A new perspective on paleopiezometry: Dynamically recrystallized grain size distributions indicate mechanism changes, Geology, 38(8), 759–762, doi:10.1130/G31162.1, 2010.

Stöckhert, B., Brix, M. R., Kleinschrodt, R., Hurford, A. J. and Wirth, R.: Thermochronometry and microstructures of quartz—

810 a comparison with experimental flow laws and predictions on the temperature of the brittle–plastic transition, Journal of Structural Geology, 21(3), 351–369, doi:10.1016/S0191-8141(98)00114-X, 1999.

Streit, J. E. and Cox, S. F.: Fluid pressures at hypocenters of moderate to large earthquakes, Journal of Geophysical Research: Solid Earth, 106(B2), 2235–2243, doi:10.1029/2000JB900359, 2001.

Stünitz, H., Fitz Gerald, J. D. and Tullis, J.: Dislocation generation, slip systems, and dynamic recrystallization in

815 experimentally deformed plagioclase single crystals, Tectonophysics, 372(3), 215–233, doi:10.1016/S0040-1951(03)00241-5, 2003.

Suominen, V.: The chronostratigraphy of southwestern Finland with special reference to Postjotnian and Subjotnian diabases, Espoo., 1991.

Torvela, T. and Ehlers, C.: From ductile to brittle deformation: structural development and strain distribution along a crustal-

820 scale shear zone in SW Finland, International Journal of Earth Sciences, 99(5), 1133–1152, 2010.

Trepmann, C. A. and Seybold, L.: Deformation at low and high stress-loading rates, Geoscience Frontiers, 10(1), 43–54, doi:10.1016/j.gsf.2018.05.002, 2019.

Trepmann, C. A. and Stöckhert, B.: Quartz microstructures developed during non-steady state plastic flow at rapidly decaying stress and strain rate, Journal of Structural Geology, 25(12), 2035–2051, doi:10.1016/S0191-8141(03)00073-7, 2003.

825 Trepmann, C. A. and Stöckhert, B.: Short-wavelength undulatory extinction in quartz recording coseismic deformation in the middle crust – an experimental study, Solid Earth, 4(2), 263–276, doi:https://doi.org/10.5194/se-4-263-2013, 2013.

Trepmann, C. A., Stöckhert, B., Dorner, D., Moghadam, R. H., Küster, M. and Röller, K.: Simulating coseismic deformation of quartz in the middle crust and fabric evolution during postseismic stress relaxation — An experimental study, Tectonophysics, 442(1), 83–104, doi:10.1016/j.tecto.2007.05.005, 2007.

830 Trepmann, C. A., Hsu, C., Hentschel, F., Döhler, K., Schneider, C. and Wichmann, V.: Recrystallization of quartz after low-temperature plasticity – The record of stress relaxation below the seismogenic zone, Journal of Structural Geology, 95, 77–92, doi:10.1016/j.jsg.2016.12.004, 2017.

Tuisku, P. and Kärki, A.: Metamorphic petrology of Olkiluoto, Posiva Oy., 2010.

Viola, G., Mancktelow, N. S. and Miller, J. A.: Cyclic frictional-viscous slip oscillations along the base of an advancing nappe

835   complex: Insights into brittle-ductile nappe emplacement mechanisms from the Naukluft Nappe Complex, central Namibia, Tectonics, 25(3), doi:10.1029/2005TC001939, 2006.

Viola, G., Venvik Ganerød, G. and Wahlgren, C.-H.: Unraveling 1.5 Ga of brittle deformation history in the Laxemar-Simpevarp area, southeast Sweden: A contribution to the Swedish site investigation study for the disposal of highly radioactive nuclear waste, Tectonics, 28(5), doi:10.1029/2009TC002461, 2009.

840   Wehrens, P., Berger, A., Peters, M., Spillmann, T. and Herwegh, M.: Deformation at the frictional-viscous transition: Evidence for cycles of fluid-assisted embrittlement and ductile deformation in the granitoid crust, Tectonophysics, 693, 66–84, doi:10.1016/j.tecto.2016.10.022, 2016.

White, J. C.: Transient discontinuities revisited: pseudotachylyte, plastic instability and the influence of low pore fluid pressure on deformation processes in the mid-crust, Journal of Structural Geology, 18(12), 1471–1486, doi:10.1016/S0191-

845   8141(96)00059-4, 1996.

White, J. C.: Paradoxical pseudotachylyte – Fault melt outside the seismogenic zone, Journal of Structural Geology, 38, 11–20, doi:10.1016/j.jsg.2011.11.016, 2012.

Yardley, B. and Baumgartner, L.: Fluid processes in deep crustal fault zones, Tectonic Faults–Agents of Change on a Dynamic Earth, 295–318, 2007.

850

Sample name	PH28_7a		PH28_7b		PH28_5a		PH28_5b		PH28_5c		PH28_5d		PH28_9		PH28_10	
N. measurement	n=5		n=5		n=15		n=18		n=12		n=16		n=8		n=10	
		s.d.		s.d.		s.d.		s.d.		s.d.		s.d.		s.d.		s.d.
SiO2	47.74	0.36	47.90	0.16	47.95	0.25	48.02	0.37	47.81	0.39	48.17	0.39	47.70	0.57	47.40	0.51
TiO2	0.08	0.01	0.08	0.03	0.09	0.03	0.07	0.04	0.06	0.04	0.10	0.03	0.16	0.14	0.11	0.05
Al2O3	34.09	0.32	34.20	0.42	34.24	0.54	34.17	0.52	34.31	0.35	34.05	0.70	34.86	0.82	34.92	0.47
Cr2O3	0.01	0.01	0.01	0.02	0.01	0.02	0.02	0.02	0.02	0.03	0.01	0.01	0.02	0.01	0.01	0.01
Fe2O3	0.00	0.00	0.00	0.00	0.00	0.00	0.00	0.00	0.00	0.00	0.00	0.00	0.00	0.00	0.00	0.00
FeO	2.38	0.24	2.37	0.14	2.21	0.29	2.25	0.18	2.21	0.14	2.24	0.46	2.89	0.21	2.63	0.00
MnO	0.03	0.03	0.03	0.02	0.02	0.02	0.02	0.02	0.03	0.02	0.01	0.02	0.03	0.03	0.02	0.02
MgO	1.49	0.07	1.38	0.05	1.38	0.15	1.47	0.12	1.41	0.04	1.45	0.21	0.99	0.47	1.35	0.11
CaO	0.01	0.01	0.02	0.01	0.07	0.19	0.02	0.02	0.03	0.03	0.02	0.01	0.01	0.01	0.03	0.02
Na2O	0.12	0.02	0.14	0.03	0.13	0.02	0.13	0.03	0.14	0.01	0.15	0.03	0.13	0.02	0.16	0.02
K2O	11.15	0.06	11.06	0.11	11.07	0.08	11.06	0.09	11.01	0.18	11.09	0.08	9.48	0.28	10.85	0.14
NiO	0.01	0.01	0.01	0.01	0.01	0.02	0.01	0.02	0.02	0.03	0.02	0.02	0.00	0.00	0.04	0.03
Structural formulae on the basis of 11 O																
		s.d.		s.d.		s.d.		s.d.		s.d.		s.d.		s.d.		s.d.
Si	3.14	0.02	3.14	0.02	3.14	0.01	3.15	0.02	3.16	0.02	3.15	0.02	3.13	0.02	3.10	0.03
Ti	0.00	0.00	0.00	0.00	0.00	0.00	0.00	0.00	0.00	0.00	0.00	0.00	0.01	0.01	0.01	0.00
Al	2.64	0.02	2.64	0.03	2.65	0.03	2.64	0.04	2.61	0.04	2.63	0.05	2.70	0.04	2.69	0.04
Cr	0.00	0.00	0.00	0.00	0.00	0.00	0.00	0.00	0.00	0.00	0.00	0.00	0.00	0.00	0.00	0.00
Fe 3+	0.00	0.00	0.00	0.00	0.00	0.00	0.00	0.00	0.00	0.00	0.00	0.00	0.00	0.00	0.00	0.00
Fe2+	0.13	0.01	0.13	0.01	0.12	0.02	0.12	0.01	0.13	0.01	0.12	0.03	0.16	0.01	0.14	0.02
Mn	0.00	0.00	0.00	0.00	0.00	0.00	0.00	0.00	0.00	0.00	0.00	0.00	0.00	0.00	0.00	0.00
Mg	0.15	0.01	0.14	0.01	0.14	0.01	0.14	0.01	0.15	0.02	0.14	0.02	0.10	0.05	0.13	0.01
Ca	0.00	0.00	0.00	0.00	0.00	0.01	0.00	0.00	0.00	0.00	0.00	0.00	0.00	0.00	0.00	0.00
Na	0.01	0.00	0.02	0.00	0.02	0.00	0.02	0.00	0.01	0.00	0.02	0.00	0.02	0.00	0.02	0.00
K	0.94	0.01	0.93	0.01	0.93	0.01	0.92	0.01	0.93	0.00	0.93	0.01	0.79	0.03	0.91	0.01
Ni	0.00	0.00	0.00	0.00	0.00	0.00	0.00	0.00	0.00	0.00	0.00	0.00	0.00	0.00	0.00	0.00

**Table 1. Average compositions EPMA of white mica along the foliation.**

Fault rock	Mylonite		Cataclasite	Veins
Sample name	PH28_10	Ph16_2	Ph28_9	P28_6
N. measurament	14	8	23	15
Chemical composition (wt%)				
SiO2	25.830	25.240	23.520	24.430
TiO2	0.081	0.038	0.086	0.057
Al2O3	21.750	22.080	23.160	21.880
FeO	29.850	30.420	36.430	36.570
MnO	0.480	0.290	1.056	0.981
MgO	12.190	11.210	5.710	6.720
CaO	0.020	0.077	0.015	0.054
Na2O	0.049	0.056	0.017	0.023
K2O	0.025	0.062	0.101	0.012
Total	90.274	89.473	90.095	90.726
Structural formulae on the basis of 14 O				
Si	2.701	2.673	2.571	2.648
Ti	0.006	0.003	0.007	0.005
Al	2.680	2.756	2.984	2.795
Fe3+	0.000	0.000	0.000	0.000
Fe2+	2.610	2.695	3.330	3.315
Mn	0.043	0.026	0.098	0.090
Mg	1.900	1.770	0.930	1.086
Ca	0.002	0.009	0.002	0.006
Na	0.010	0.011	0.004	0.005
K	0.003	0.008	0.014	0.002
XFe= Fe/(Fe+Mg)	0.579	0.604	0.782	0.753

Table2. Representative chlorite EPMA for structural zones of fault core of BFZ045.

(a)

(b)

Migmatites TTG-style granitoids Granitic pegmatite

D₄ deformation zone —— Fault zone
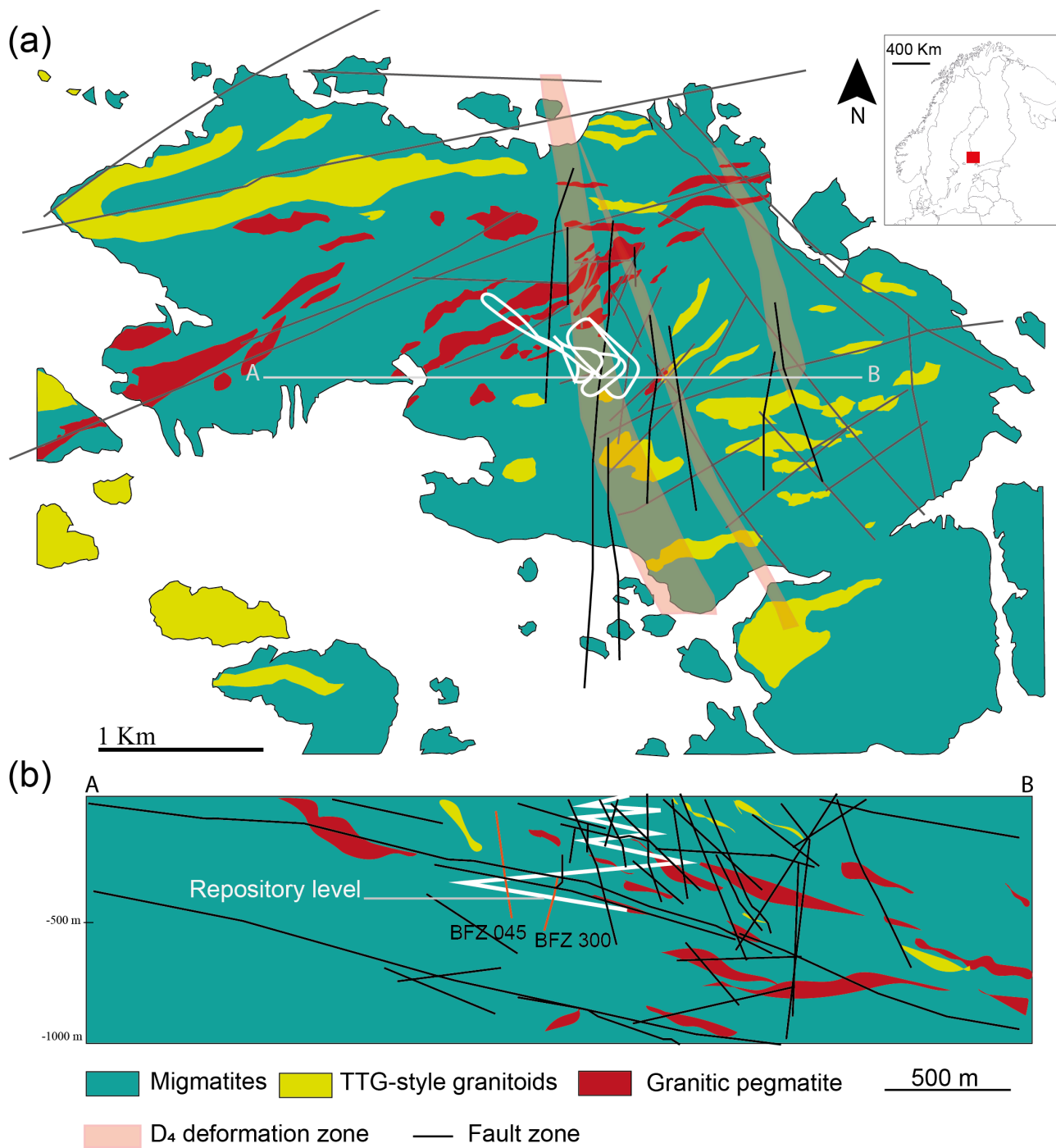
Figure 1. Geological setting of Olkiluoto, SW Finland (inset on top-right). (a) Schematic geological and structural map, showing surface intersection of modelled brittle fault zone (BFZ) and ductile deformation zone, modified from Aaltonen et al. (2016) and Skytta and Torvela (2018). The white line indicates the location of the underground Onkalo facility. A-B is the trace of the cross section shown in (b). (b) East-west cross section across the underground infrastructure, with the tunnel shown as white line. Sub vertical fault BFZ045 described in this study and its conjugate BFZ300 are shown as orange lines.
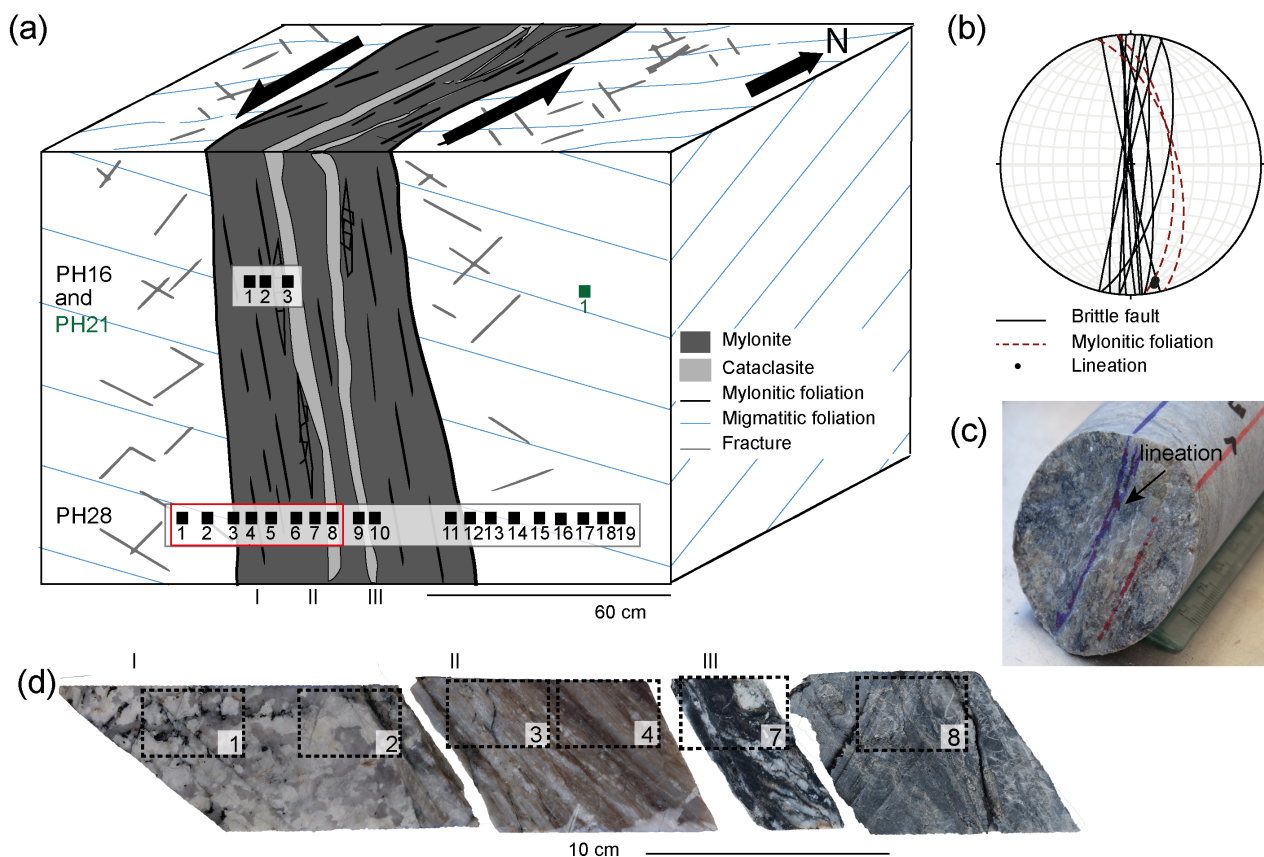
Figure 2. BFZ045 fault geometry. (a) Schematic representation of fault architecture from core logs, vertical axis not to scale. Grey rectangles locate the studied drill cores PH28 and PH16, black squares show sample location. The red rectangle indicates the samples shown in (d). (b) Stereoplot of BFZ045 fault core orientation and mylonitic foliation observed at different drill hole intersection along the Onkalo facility (Aaltonen et al., 2016). (c) Core sample along PH28 drill core within the fault core unit. The core sample exposes the mylonitic foliation, where the blue line indicates the stretching lineation, which is parallel to chlorite striae. The red line indicates the lower part of the core (d) Samples from PH28 drill core representative of the fault units: damaged coarse-grained host rock (I), and fault core with mylonites and chlorite rich cataclasites (II-III). Dashed lines outline the area of petrographic thin sections.
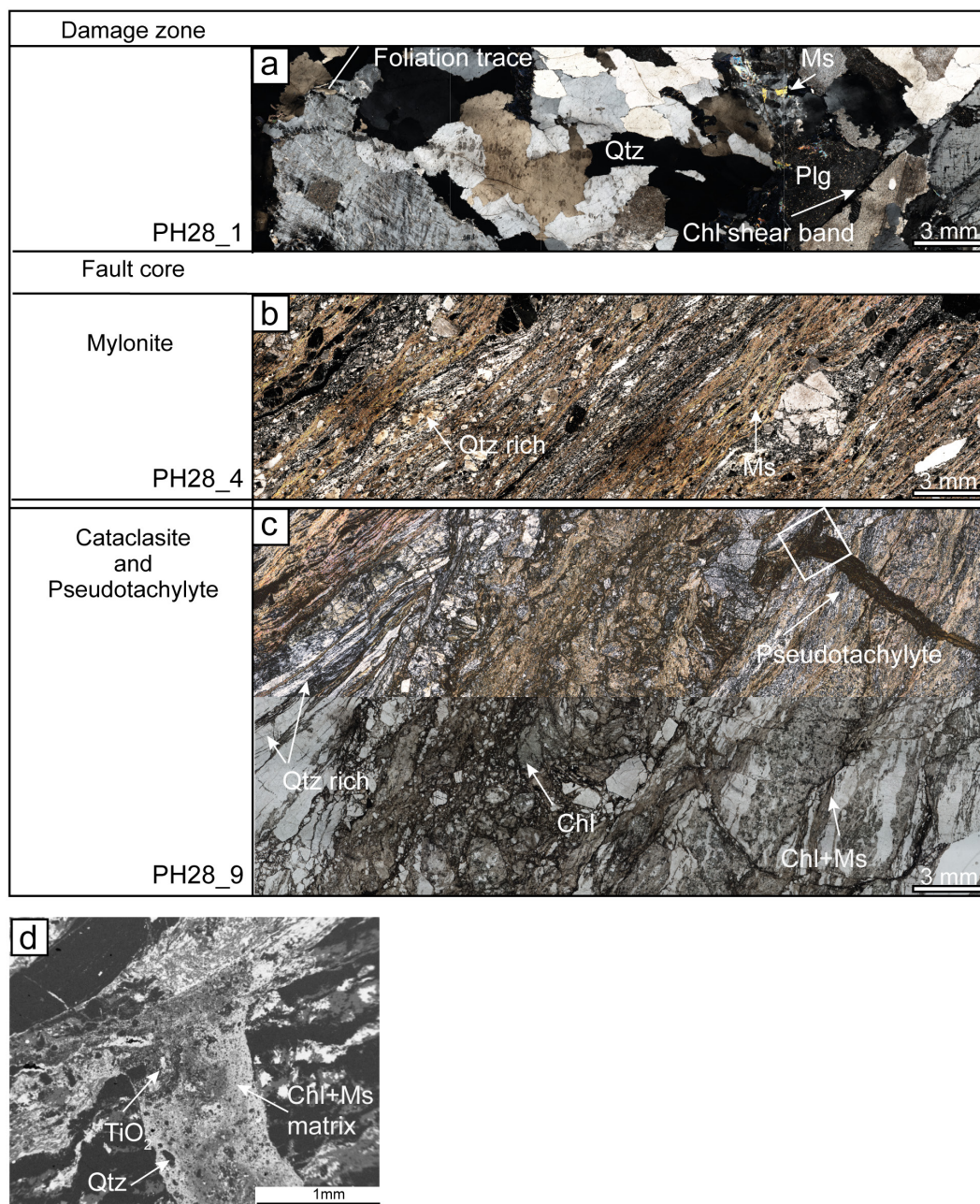
Figure 3. Polarized light microscope images of characteristic lithologies for the damage zone (a) and fault core (b-c). Stitched microphotographs in cross-polarized light and plane polarized light. (a) Damage zone shows the original magmatic textures and mineral assemblage of the host rock. White arrow shows a chlorite-rich shear band oriented at a low angle to the mylonitic foliation of the fault core. (b) Mylonite in the fault core. Foliation is defined by the alternation of quartz-rich and mica-rich domains. Porphyroclasts of feldspars are preferentially located in mica-rich domains. (c) Fault core cataclasite with characteristic pseudotachylyte injection veins (arrow). The cataclasite matrix is enriched in chlorite and Ti-oxides. (d) Scanning electron microscope (SEM) image of the pseudotachylyte injection vein. Rounded quartz clast (dark grey) and Ti-oxides (white) are surrounded by a chlorite and mica rich ultrafine grained matrix.

31
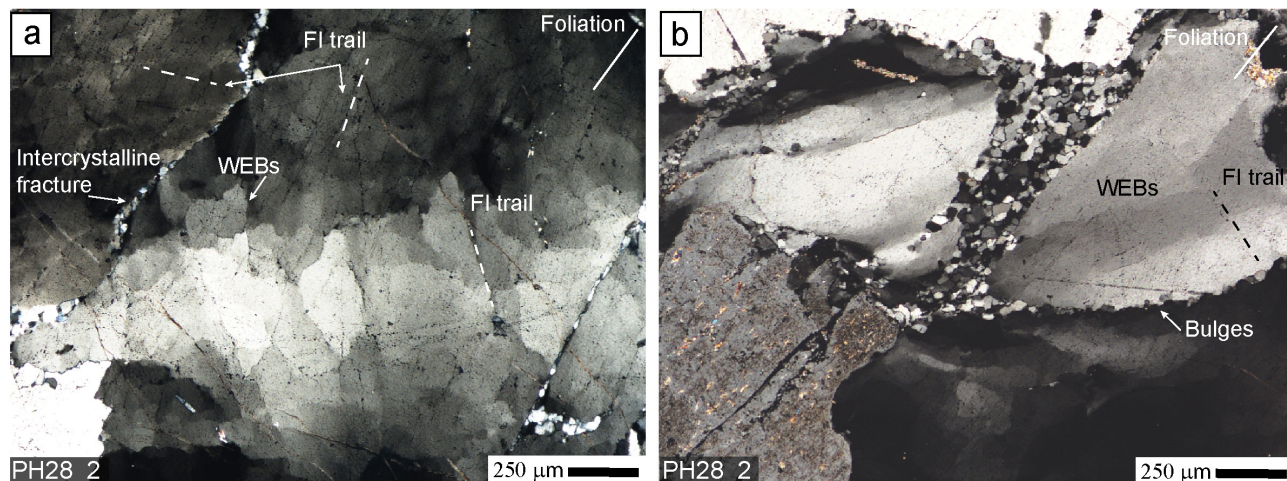
Figure 4. Quartz microstructures in the damage zone. Cross polarized light. (a) Quartz with wide extinction bands (WEBs) and undulatory extinction. WEBs are bounded by sets of fluid inclusions trails (FI trail, dashed lines). Intercrystalline deformation bands and well-developed FI trails developed sub-parallel to the foliation. (b) Polygonal recrystallized quartz grains, with small grain size (~20 μm), forming bands oriented sub-parallel to the foliation. The white arrow shows sutured grain boundaries between magmatic quartz grains, indicative of bulging.

885
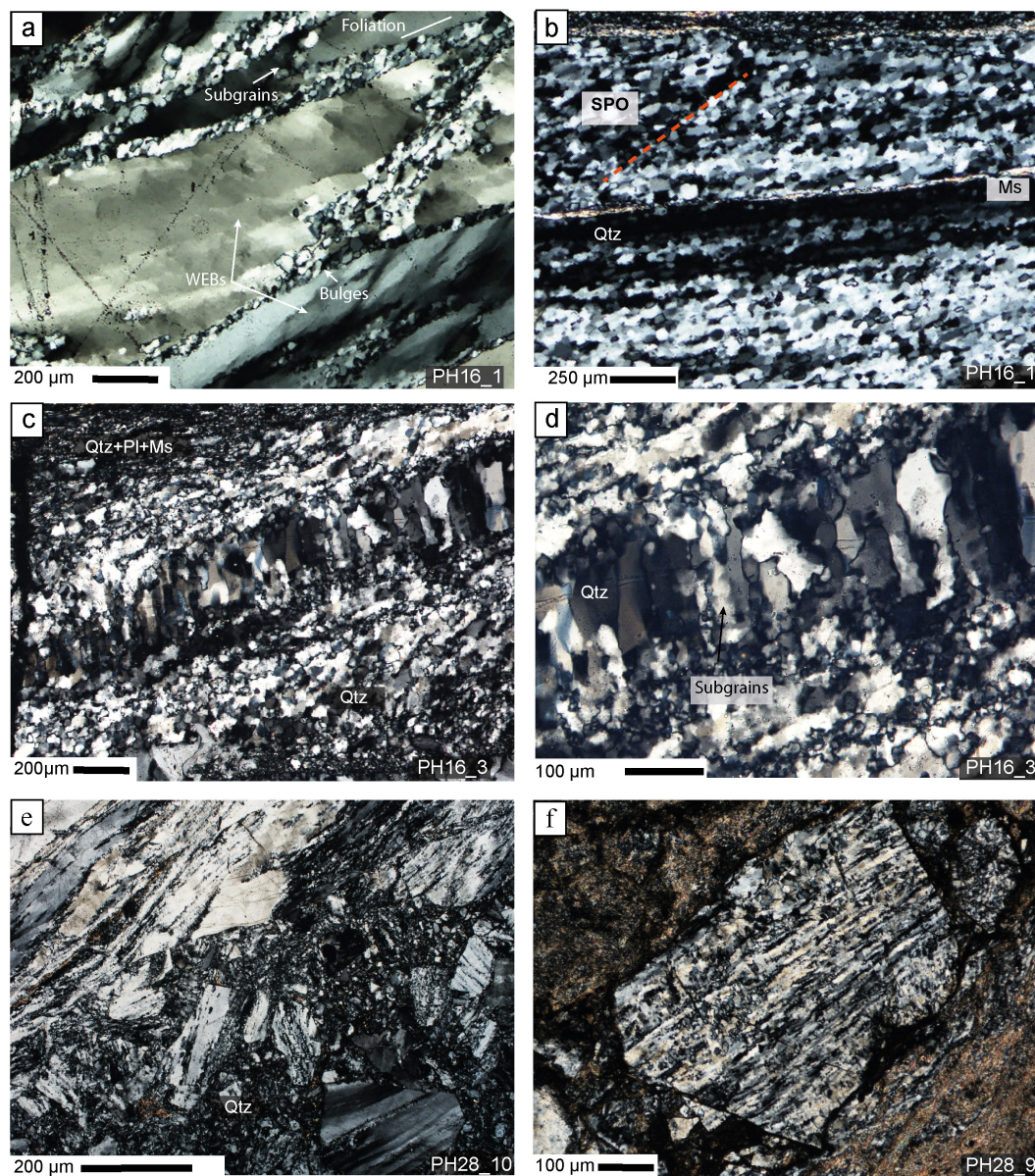
Figure 5. Quartz microstructures in the fault core. Microphotograph in cross polarized light. (a)Quartz ribbons in the shear zone boundary are stretched along the foliation and show typical core-and-mantle microstructure, with recrystallization localized at the grain boundaries. Ribbons contain also well-developed WEBs. (b) Completely recrystallized quartz ribbon. The recrystallized grains show a shape preferred orientation indicating a sinistral sense of shear. Thin muscovite (Ms) layers define the mylonitic foliation, together with the elongated and recrystallized quartz domains. (c) Quartz veins along the foliation, infilling of a mode I fracture at a distance of ~ 1cm from the cataclasite fault core. Quartz grains elongation in the veins is normal to the vein wall and to the foliation. (d) High magnification view of the quartz infilling the vein. Bulges along the grain boundaries, and subgrains within the grains are visible. (e) Contact between the mylonite and the cataclasite. Quartz form almost entirely recrystallized polycrystalline ribbons. (f) Detail of a sub-angular polycrystalline clast of quartz in the cataclasite.The trace of the mylonitic foliation is still visible in the clast, and is only slightly rotated with respect to the trace of the foliation in the mylonite. The surrounding matrix is a fine mixture of white mica and plagioclase.
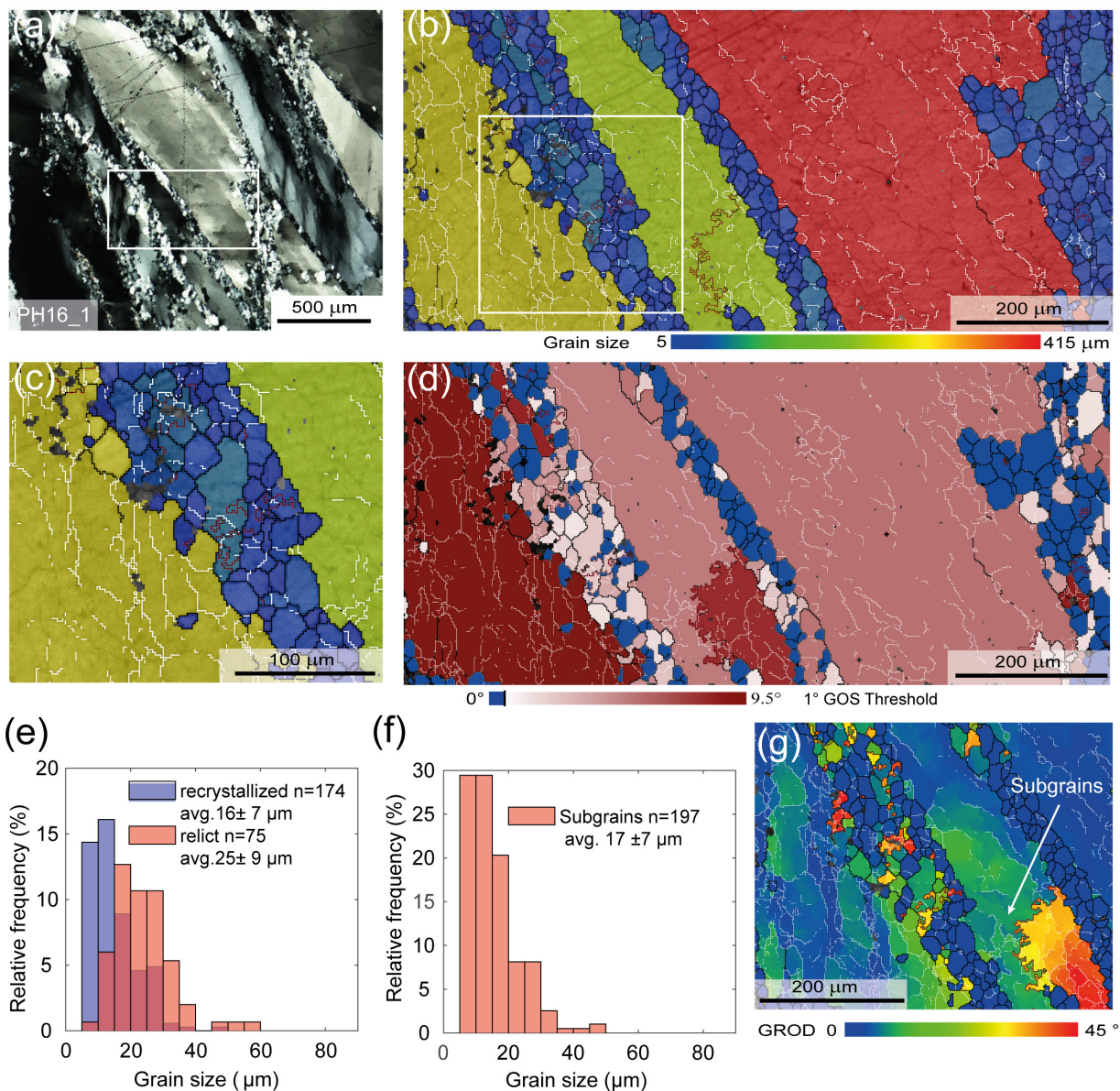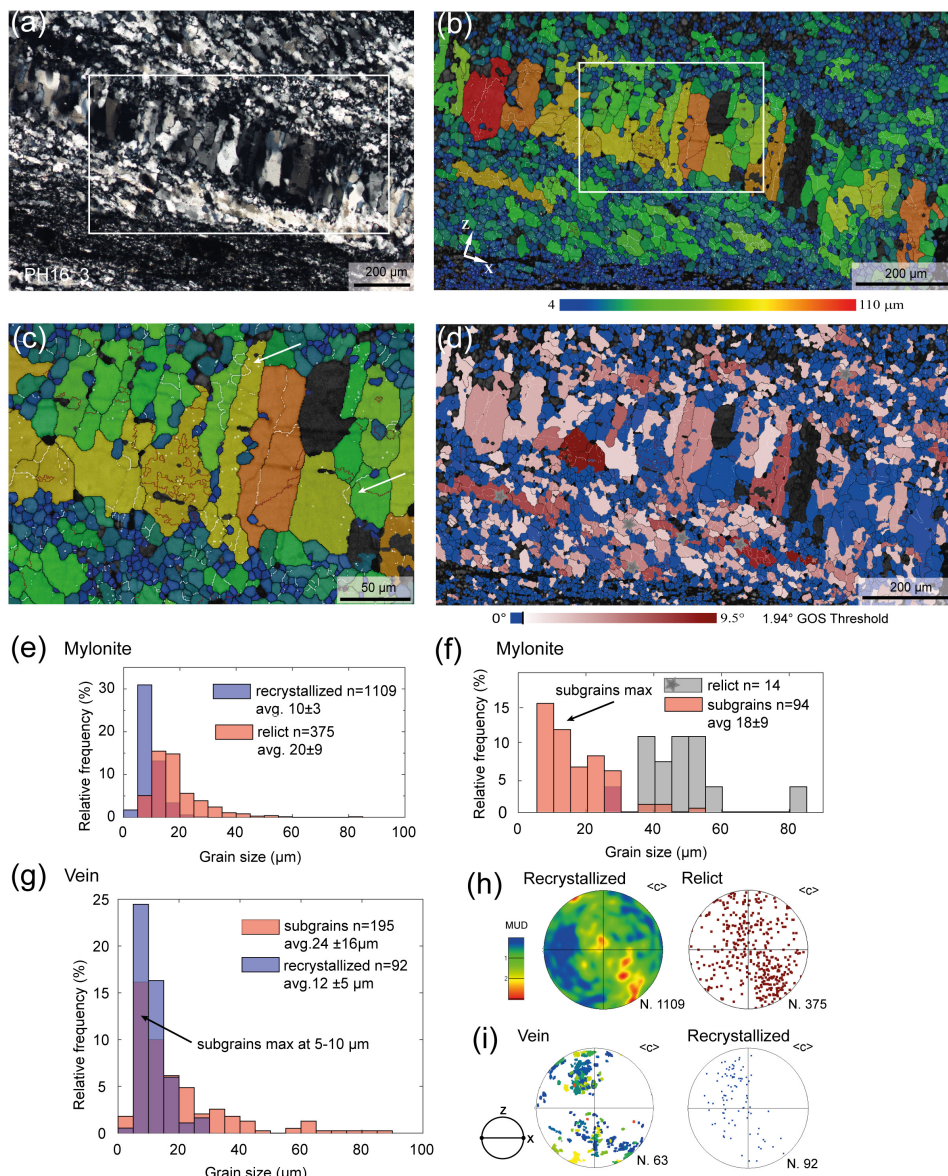
Figure 6. EBSD data of quartz from the mylonitic fault core. In all the EBSD maps, black lines correspond to high-angle boundaries (misorientation > 10°), white lines to low-angle boundaries (misorientation between 2° and 10°), and red lines to Dauphiné twin boundaries (misorientation of 60° around the c-axis). (a) Quartz ribbons and intracrystalline bands of recrystallized grains (Fig. 5a). Cross polarized light. The box locates the EBSD map shown in (b-d, g). (b-c) Grain size map (diameter of the equivalent circle, µm), the higher magnification in (c) highlights the presence of subgrains in the large relict quartz grains and in the recrystallized grains. (d) Grain orientation spread (GOS) for each grain, coloured relative to the GOS threshold (black line) between recrystallized (blue) and relict (red) grains. (e) Histogram of grains size distribution of grains in the intercrystalline bands. (f) Histogram of subgrains size distribution of subgrains in the relict quartz from the intercrystalline bands (light red in (d)). (g) Grain Orientation Distribution maps (GROD) was used to estimate visually the subgrains size in the quartz ribbon.
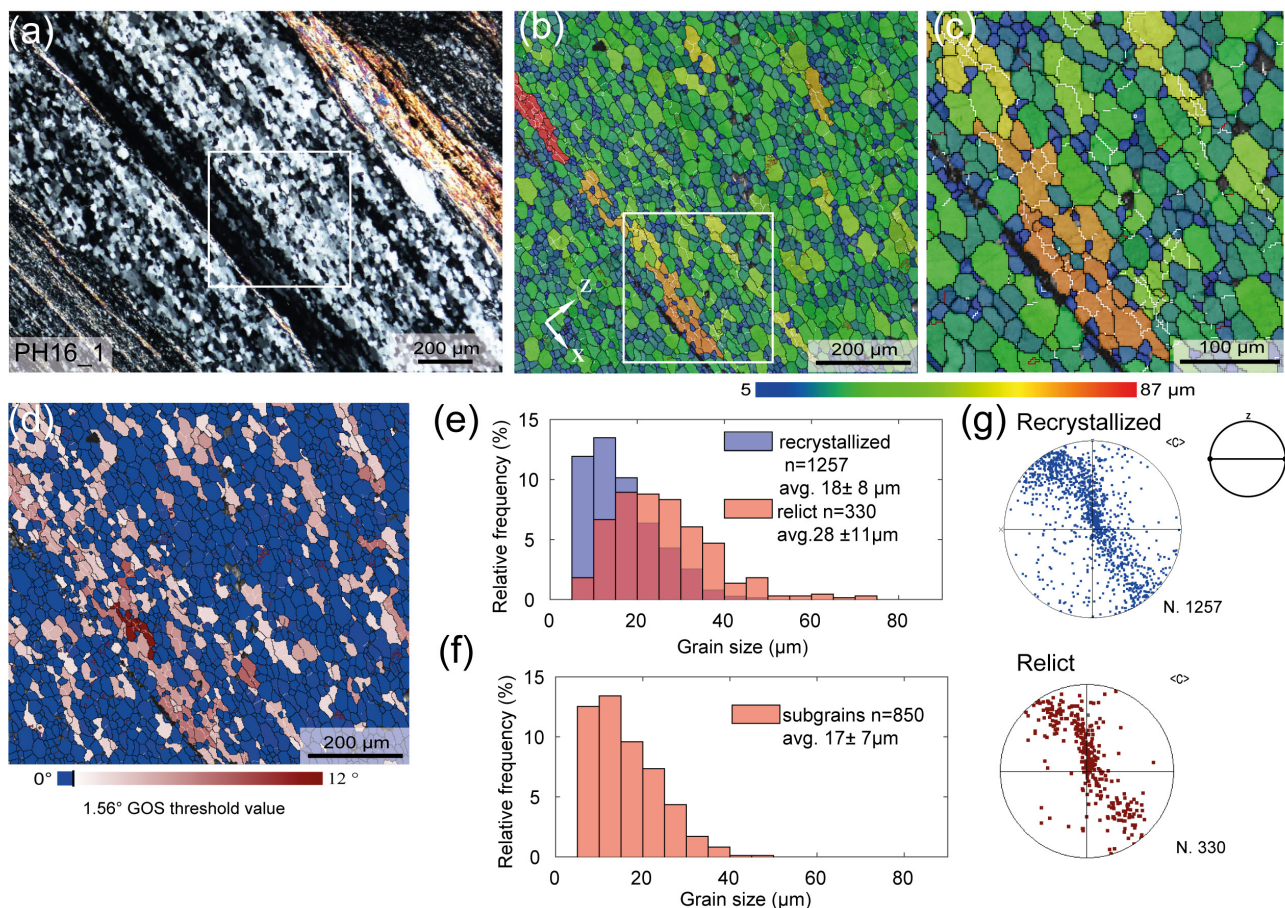
Figure 7. EBSD data of quartz from a recrystallized ribbon in the mylonite. (a) Polycrystalline ribbons of recrystallized quartz grains elongated parallel to the mylonitic foliation (Fig. 5b). Cross polarized light. The box indicates the EBSD maps shown in (b-d). Colour coding of the boundaries like in Figure 6. (b, c) Grain size map (diameter of the equivalent circle, μm) and detail (c) showing that the larger grains contain subgrains of the same size as the surrounding finer grains.(d) GOS map showing that the GOS values are mostly under the threshold, indicative of high degree of recrystallization. (e) Histogram of the grain size distribution for recrystallized and relict grains. (f) Histogram of the subgrain size distribution in the relict quartz grains identified in (d) and (e).(g) Pole figure of the c-axis orientation of recrystallized and relict grains, colour coded like the GOS map in (d). Equal area, lower hemisphere projection.

35

Figure 8. EBSD data of quartz from a foliation-parallel vein in the mylonite near the contact to the cataclasite. Colour coding of the boundaries like in Figure 6. (a) Quartz vein along the foliation. Quartz in the mylonite show a strong SPO consistent with the sinistral sense of shear of BFZ045. Cross polarized light. (b) Grain size map (diameter of the equivalent circle, µm. (c) Details of previous maps. Bulges and subgrains (white arrows) of similar size of the bulges are evident within the vein quartz. (d) GOS map of quartz in the vein and of the surrounding mylonite. The GOS threshold value of 1.94° separates relict grains (red) from recrystallized grains
925 **(blue).Grey stars indicate relict grains plotted in (f) for subgrain size estimates. (e) Histogram of the grain size distribution in the mylonite, with relict and recrystallized grains separated with the GOS method. (f) Histogram of the subgrain size distribution (red) in relict quartz of the mylonite (grey). (g) Histogram of the recrystallized grain size (red) and subgrains size (blue) distribution in the vein. (h-i) Pole figures of the c-axis orientation of the recrystallized and relic quartz in the mylonite (h) and in the veins (i). Equal area, lower hemisphere projection.**
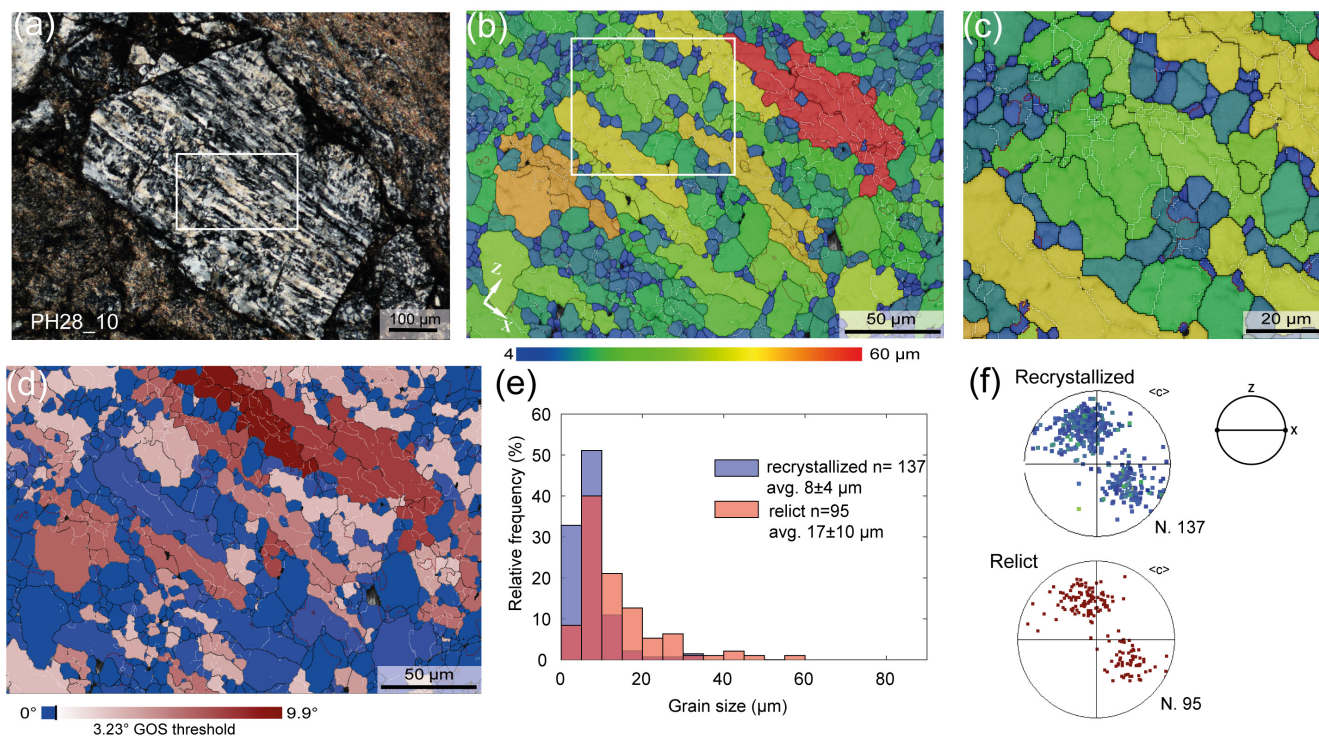
930

Figure 9. EBSD data of quartz from a clast in the cataclasite. Colour coding of the boundaries like in Figure 6. **(a)** The analysed quartz clast (Fig. 5f). The white rectangle locates the EBSD map shown in (b-d). **(b-c)** Grain size map (diameter of the equivalent circle, µm). The map highlights the presence of subgrains in the coarser elongated quartz grains with size comparable to the surrounding finer quartz. **(d)** GOS map. **(e)** Histogram of the grain size distribution of the recrystallized (blue) and relict (red) grains. **(f)** Pole figure of the c-axis orientation of recrystallized and relict grains. Equal area, lower hemisphere projection, color coded as GOS map.
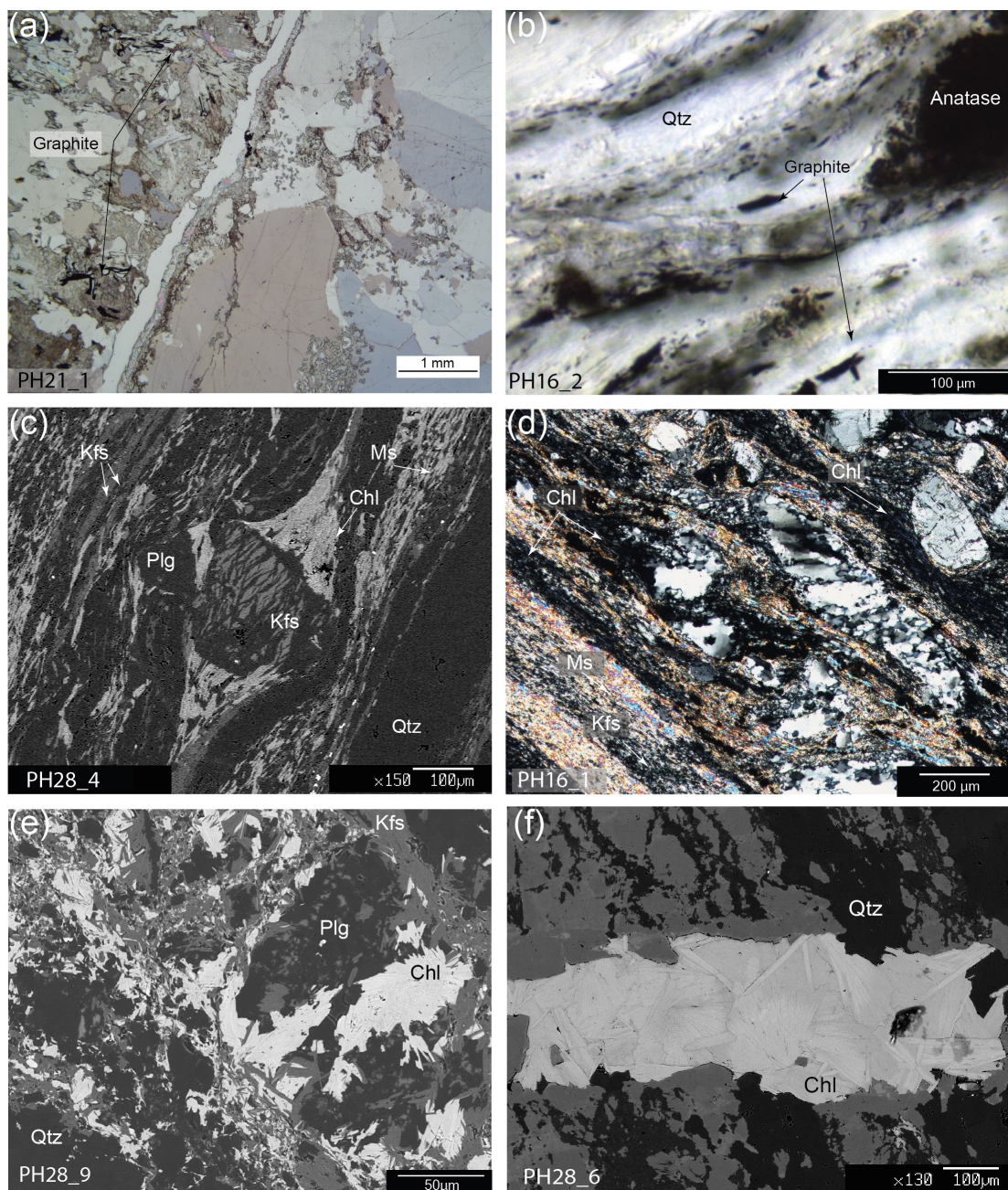
Figure 10. Light microscopy and SEM backscattered electron (BSE) images of characteristic microstructural domains and mineral assemblages used for geothermobarometry estimates. (a) Graphite flakes in association with radiate chlorite in the host rock. Plane polar light. (b) Detail of graphite grains along the mylonitic foliation of BFZ045. Plane polar light. (c) Chlorite in pressure shadows around a K-feldspar porphyroclast in the mylonite. White mica and a fine grained recrystallized K-feldspar assemblage is common along the foliation. (d) Light microscope image of a microstructure similar to (c), cross polar light. (e-f) SEM BSE images of radiate chlorite used for chlorite thermometry in the cataclasite matrix (e) and in a vein cutting the mylonitic foliation (f). The trace of the mylonitic foliation in (f) is oriented ca. NW-SE.
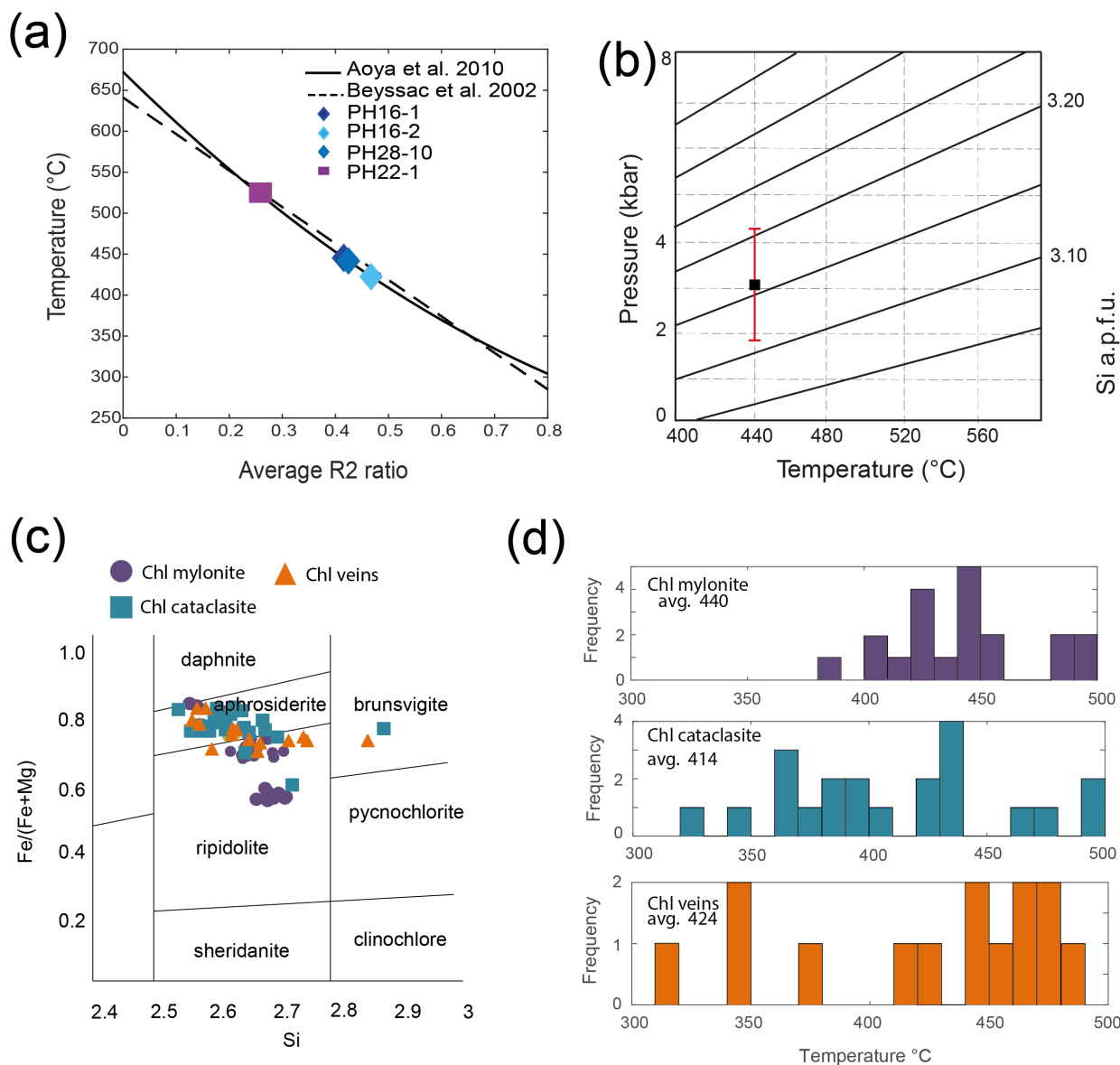
945

Figure 11. Results of P-T estimates. (a) Carbonaceous material Raman geothermometer. Average R2 ratio (refer to text for explanation) for graphite rich mylonitic and host rock samples was measured to derive a T estimate using the method of Beyssac et al. (2002) and Aoya et al. (2010). (b) Estimated P of mylonitization using the Si-in-phengite barometer (Massonne and Schreyer, 1987) for the average T of 440° C obtained with the carbonaceous material Raman thermometry.Red line show the total spread of the Si values obtained. Black square show the (c) Chlorite compositional diagram based on Hey (1954). (d) Chlorite formation temperature estimated for mylonitic foliation, veins and cataclasite using the method of Lanari et al. (2014).

950
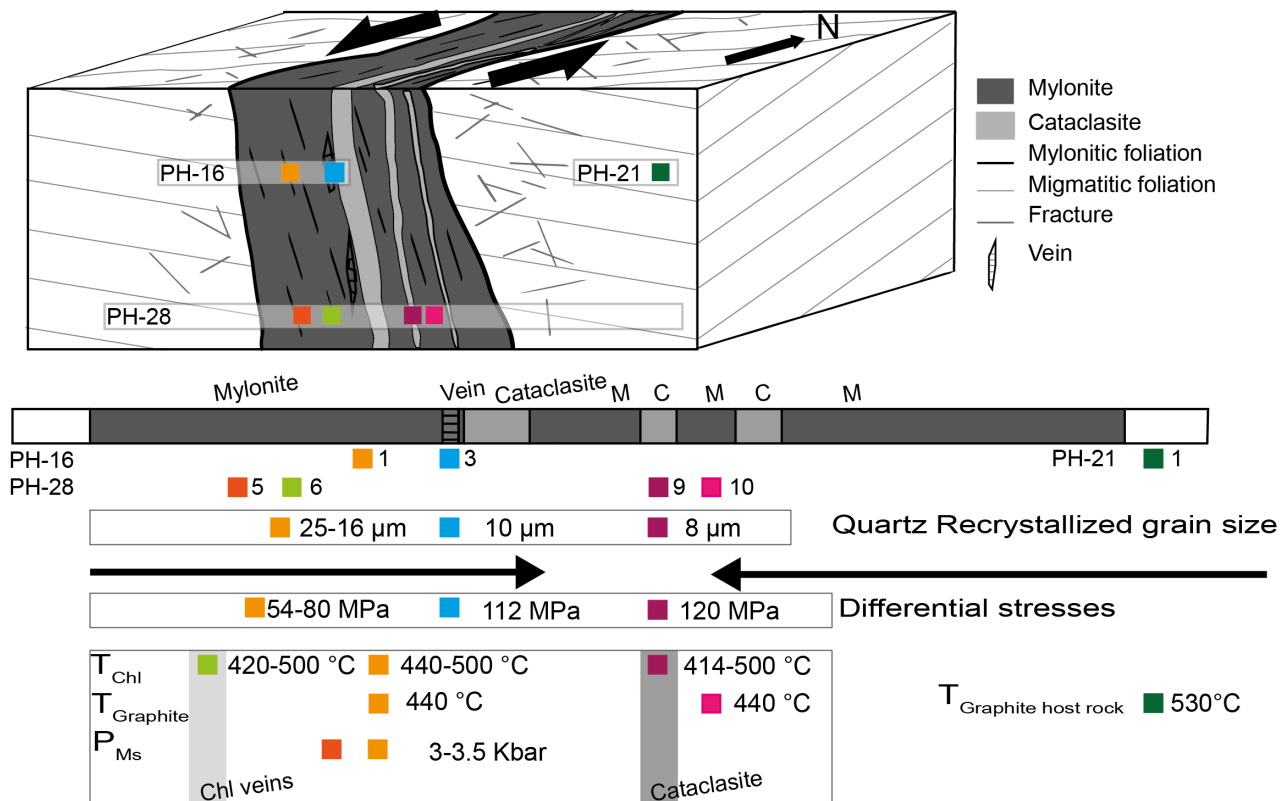
Figure 12. Schematic summary of the quartz recrystallized grain size, differential stresses, and P–T conditions of deformation for BFZ045 derived in the present study, in relationship to the fault core geometry. Each sample is coloured differently to indicate the spatial position of the results described in section 4 of this paper.
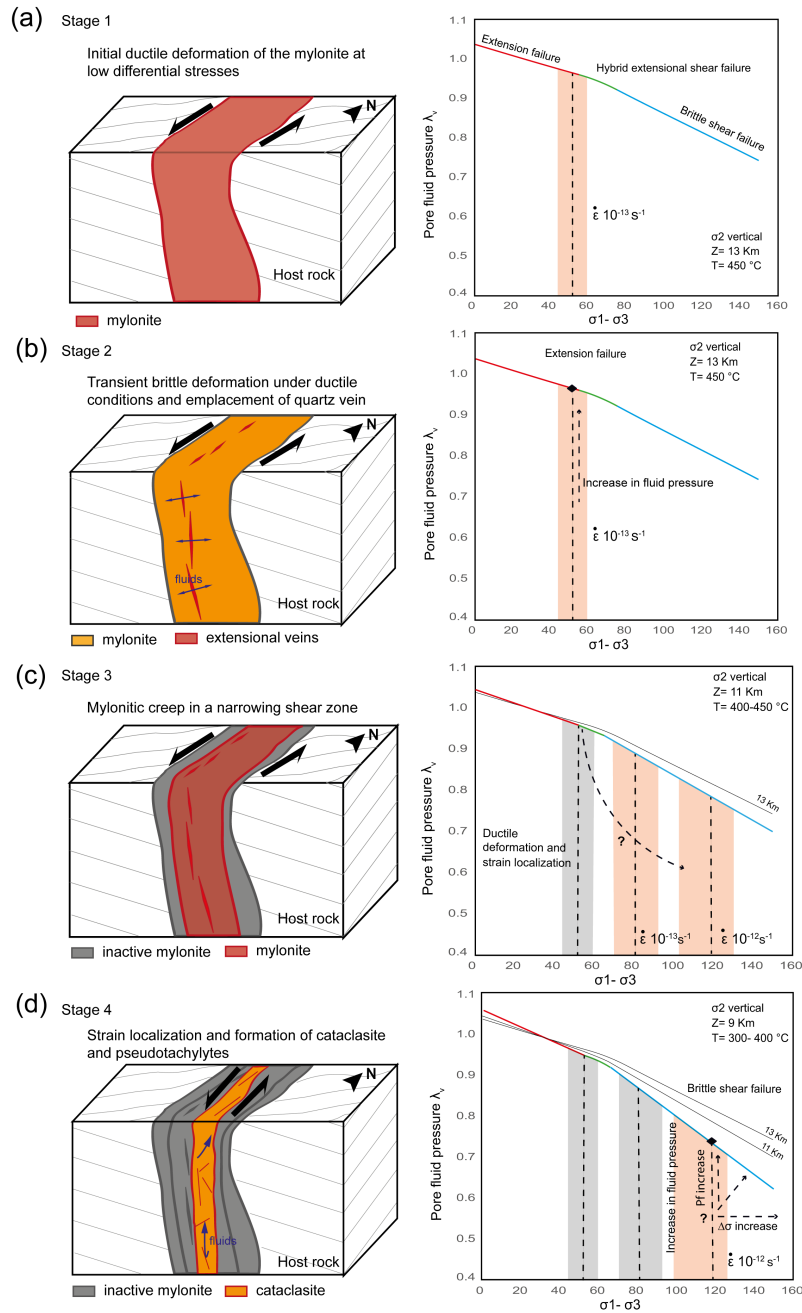
955

Figure 13. Conceptual model of the temporal and mechanical evolution of the BFZ045 fault zone (see text for more details). Grey lines: traces of metamorphic foliation in the host rock. In the schematic fault scheme evolution, red displays the active deformation process, grey represents the inactive deformation processes, and orange suggests a transition in the deformation. BFZ045 was characterized by (a) the development of mylonite under low differential stress followed by (b) a transient increase in fluid pressure responsible for the emplacement of quartz vein. (c) Progressive exhumation and cooling resulted in strain localization toward the centre of the mylonitic fault core in an overall narrowing shear zone, with subsequent deformation of the fault under brittle condition and associated formation of cataclasite and pseudotachylyte (d).